Modeling Mars' ionosphere with constraints from same-day observations by Mars Global Surveyor and Mars Express

Michael Mendillo,[1,2] Anthony Lollo,[1,2] Paul Withers,[1,2] Majd Matta,[1,2] Martin Pätzold,[3] and Silvia Tellmann[3]

Received 23 May 2011; revised 18 July 2011; accepted 3 August 2011; published 2 November 2011.

[1] We have analyzed a brief period of same-day observations of the Martian ionosphere using data obtained in December 2004 from the Mars Global Surveyor (MGS) and Mars Express (MEX) radio occultation experiments. These data were taken shortly after sunrise under solstice conditions in both hemispheres, with MGS in the summer (northern) hemisphere at high latitudes while MEX was in the winter (southern) hemisphere at midlatitudes. Such two-satellite, dual-hemisphere data sets are unique for the modern era of ionospheric observations at Mars and provide good test cases for constraints of key parameters commonly used in models of the Martian ionosphere. Several iterations of a 1-dimensional model are developed in attempts to simulate more successfully the altitudes, absolute magnitudes and shapes of the two photo-chemical layers (M1 and M2) obtained during the joint MGS-MEX observing period. Three basic processes are examined: (1) selection of the optimal model neutral atmospheres, (2) the effects due to departures from thermal equilibrium between electrons, ions and neutrals, (3) methods of handling secondary ionization. While general circulation models fully coupled to plasma transport codes are required for global simulations of the full system, the computational complexity and computer resources needed often result in the use of parameterizations relating electron and ion temperatures to neutral temperatures and secondary ionization to primary photo-ionization profiles. Here we develop such schemes and test them within the framework of same day observations in both hemispheres. The occurrence of same day, separate hemisphere, radio occultation profiles is important because the solar irradiance has to be held constant for modeling both sites, and thus this is the first study of this kind to be done. The overall results stress the dominant influence of solar zenith angle effects on production for the M2-layer via primary solar ionization, its augmentation by ~30% due to secondary ionization, and further enhancements due to reduced chemical loss when the electron temperature exceeds the neutral temperature. Secondary ionization is the most crucial process for the M1-layer. The influence of very different crustal magnetic field morphologies at the two observing locations did not seem to be a crucial source of differentiation for processes that control the average values of the peak electron densities of the two photo-chemical layers.

Citation: Mendillo, M., A. Lollo, P. Withers, M. Matta, M. Pätzold, and S. Tellmann (2011), Modeling Mars' ionosphere with constraints from same-day observations by Mars Global Surveyor and Mars Express, *J. Geophys. Res.*, *116*, A11303, doi:10.1029/2011JA016865.

1. Introduction

1.1. Discovery Era Theory and Observations

[2] Models of the Martian ionosphere predate missions to Mars. *Chamberlain* [1962], for example, made calculations of four possible ionospheric layers on Mars that had peak densities in the 10^4–10^5 e^- cm^{-3} range. Due to a lack of knowledge about the temperature profile and neutral compositions, the altitudes of these layers were from ~130 km to greater than 700 km. Subsequent observations of the electron density profiles at Mars were made by a series of radio occultation experiments on flyby missions and then by orbiting spacecraft and the Viking landers. From the first observation on 14 June 1965 by the Mariner-4 flyby [*Kliore et al.*, 1965] to the last profile of 17 August 1980 from the Viking-1 orbiter [*Lindal et al.*, 1979; *Kliore*, 1992], there were 433 electron density profiles in the published literature [see *Mendillo et al.*, 2003, Table 1]. These data spanning

[1]Department of Astronomy, Boston University, Boston, Massachusetts, USA.
[2]Center for Space Physics, Boston University, Boston, Massachusetts, USA.
[3]Rheinisches Institut für Umweltforschung, Abteilung Planetenforschung, University of Cologne, Cologne, Germany.

0148-0227/11/2011JA016865

~15 years sampled the Martian ionosphere over many latitudes, longitudes, local times, seasons and solar cycle conditions. The two most comprehensive data sets came from the Viking-1 and 2 landers in 1976 that measured descent profiles of the neutral and ionized compositions and plasma temperatures [*Nier and McElroy*, 1976; *Hanson et al.*, 1977; *Hanson and Mantas*, 1988]. Yet, the sparse coverage provided by 433 observations over ~7 $\frac{1}{2}$ Martian years offered no chance of continuity for morphology studies in space or time, and thus model-data comparisons were limited to single-site, case studies only.

[3] The ionospheric compositions from the Viking landers have been modeled by *Chen et al.* [1978] and *Fox* [1993], as have the plasma temperatures by *Choi et al.* [1998]. In their descent to the surface, the Viking probes showed a main ionospheric layer with an electron density of ~10^5 e^- cm^{-3} near 130 km. This in situ finding of peak electron densities between 125 and 140 km was a feature found regularly by the 431 radio occultation experiments before and after. Yet, the radio occultation measurements most often showed a secondary layer, or ledge, near 110 km with electron density ~3×10^4 e^- cm^{-3}. There was no evidence for this secondary layer in either of the Viking descent profiles. All 1-dimensional models shared a broad agreement on the existence of two solar produced photochemical layers, with the lower Martian layer (M1) due to soft X-rays and the main layer (M2) due to solar EUV [see *Fox and Yeager*, 2006; *Fox et al.*, 2008, and references therein]. As the 20th century drew to its end, the lack of new data created serious impediments to progress, not only for modeling constraints, but also for the study of ionospheric variability.

1.2. Next Generation Observations

[4] A new era of Martian ionospheric measurements began in December 1998 when the radio occultation experiment onboard Mars Global Surveyor (MGS) [*Hinson et al.*, 1999, 2000] began a series of observations that ultimately led to 5600 profiles by mission end in November 2006. This MGS database thus increased the 'discovery-era' (1965–1980) observational coverage by more than a factor of ten in just 7+ years of operation.

[5] In 2003, two radio wave experiments on the Mars Express (MEX) mission arrived at Mars: a radio occultation experiment (Mars Radio Science, MaRS) that began operations in April 2004 [*Pätzold et al.*, 2005] and the Mars Advanced Radar for Subsurface and Ionospheric Sounding (MARSIS), a topside sounder experiment that began in June 2005 [*Gurnett et al.*, 2005]. The MGS and MEX radio occultation experiments measure the full electron density profile (i.e., above and below the altitude of peak density, N_{max}, of the M2-layer), while the MARSIS experiment obtains reflections at plasma frequencies up to the penetration frequency (i.e., from the height of the satellite down to the peak electron density of the M2-layer).

[6] Among the major discoveries to come from the increased availability of observations enabled by MGS and MEX radio occultation methods, two were the identifications of transient enhancements of electron densities in the Martian ionosphere: (1) *Pätzold et al.* [2005] found a set of MEX profiles that had an additional plasma structure below the M1-layer, a characteristic that pointed to meteoritic origin. A follow-up study using MGS data that showed similar sporadic, low-altitude ionospheric layers attributed to meteoroids was conducted by *Withers et al.* [2008]. (2) Solar flares have also produced ionospheric signatures at Mars. The first detection of a flare-associated ionospheric enhancement in the solar EUV produced M2-layer was reported using MEX data by *Gurnett et al.* [2005]. The stronger effects of solar flare X-rays upon the M1-layer were reported by *Mendillo et al.* [2006] using MGS radio occultation data, and a follow-up case has been described by *Haider et al.* [2009]. In non-radio occultation experiments, *Gurnett et al.* [2010] used MARSIS to study ionopause signatures (or lack thereof), and *Morgan et al.* [2011] have recently reported on dual-spacecraft (MEX and MGS) observations of flux ropes in the Martian ionosphere.

[7] When additional sources of ionization occur (from meteoroids, flares or energetic particles), they augment the normal day-to-day variability produced by solar irradiance changes. A recent summary of all such forms of observed variability appears in work by *Withers* [2009]. To date, only the daily irradiance mechanism has been subjected to model studies [*Martinis et al.*, 2003]. The goal of this study is to revisit the photo-chemical processes that have long been known to be responsible for the lower (M1) and higher (M2) ionospheric layers with the aim of recasting them within a framework of flexibility suitable for data-model comparisons under a broad range of conditions. Our emphasis will be on the M1 and M2 layer peak densities, heights and profile shapes, leaving the topside ionosphere (where both chemistry and transport are important) for future study. This will enable future studies of transient variability sources that affect the M1 and M2-layers to rest upon validated methods of modeling the ambient ionosphere near and below its altitude of peak electron density.

1.3. Simultaneous Data From Two Spacecraft

[8] The fact that the MGS and MEX radio occultation experiments obtain similar types of data, and were in operation for a brief overlap period (8 December 2004 to 4 January 2005), makes this pair well suited for "dual-site" model-data comparisons. Other satellites, of course, obtained data on the same day (e.g., all of the flybys that had both ingress and egress observations, as well as prior orbiting satellites, had multiple results within a single day). To our knowledge, however, such data were never used to constrain models by the requirement of the same solar irradiance for that day being applied at two locations. Fixing solar input at both sites allows us to explore additional parameters and mechanisms within a highly coupled system. This is especially relevant for the bottom-side layer (M1) that is so dependent upon secondary ionization. Moreover, the MGS and MEX profiles relate to different hemispheres (summer and winter solstices), and thus serve to constrain photochemical theory simultaneously for different solar zenith angles on the same day.

2. Radio Occultations by Two Spacecraft

[9] The radio science (RS) occultation experiment on MGS has been described by *Hinson et al.* [1999, 2000, 2001]. The data reduction method is the classic 'onion peel' inversion method that assumes a spherically symmetrical and time invariant $N_e(h)$ profile probed by a raypath's

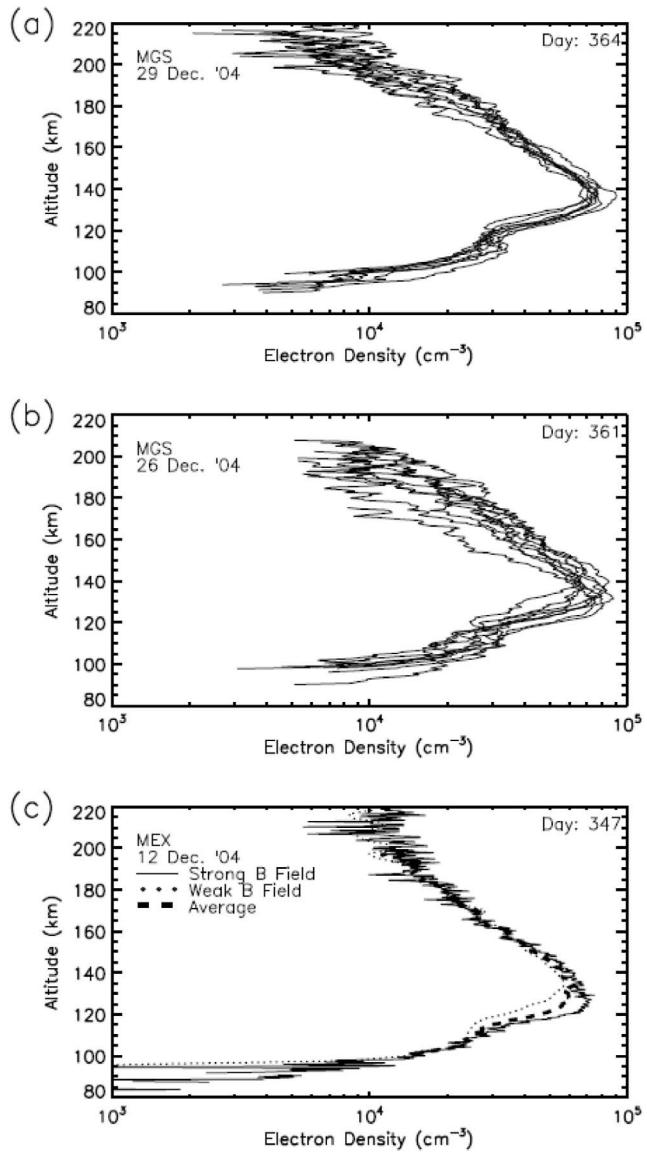

Figure 1. Examples of electron density profiles obtained by two radio occultation experiments during a common period of observation between 8 December 2004 and 4 January 2005 (see text). (a) MGS observations of 8 profiles on 29 December (a day with low variability); (b) 9 MGS profiles on 26 December (with higher variability). (c) MEX observations of 2 profiles (solid and dotted lines) on 12 December with the daily mean shown (thick dashed line). The MEX profile on the right occurred at a location with strong crustal magnetic fields (see text).

passage through the ionosphere as the satellite goes into/out of eclipse as seen from Earth. There is no a priori assumption about the shape for the electron density profile or its peak altitude, but the electron density is assumed to be zero below a floor height, typically 90 km. The resultant uncertainty in magnitude for a single experiment is typically several thousand e^- cm^{-3}. In the course of a UT day, there can be several MGS radio occultation opportunities (up to 13). The MGS orbit results in these events producing $N_e(h)$ profiles that have very similar latitudes and local times (i.e., only the longitude changes). During the 28-day overlap period of interest here, the MGS occultations occurred at high latitudes in the northern hemisphere on 25 of those days, under summer solstice conditions (Ls = 125°–139°), at early local times in the Martian day. The observed variations of the M1 and M2 electron densities with longitude at high latitudes in the northern hemisphere are in the 5–10% range [*Haider et al.*, 2006], and thus we assume coherence and average all profiles on a single day to form the daily mean profile for that latitude and local time. There are known variations in longitude of the heights of the M1 and M2 layers [*Bougher et al.*, 2001, 2004] which we assume do not affect an average formed from 8 to 13 profiles per day distributed in longitude. The average latitude for the 25 days of MGS data was 70°N with mean local time of 05:00, corresponding to a solar zenith angle of 77°.

[10] The MEX radio occultation experiment and its data analysis methods (similar to those used for MGS) have been described by *Pätzold et al.* [2004, 2005]. It was during their second "occultation season" of December 2004–January 2005 that the overlap with MGS occurred. The Mars Express spacecraft has a far more elliptical orbit than MGS, and thus there was generally a single $N_e(h)$ profile obtained each day, with only a few cases of multiple profiles per day. The observations all pertain to the southern hemisphere (winter solstice), span lower to upper midlatitudes, and again occur early in the local time day at Mars. Many of the profiles prior to dawn suffered from low electron densities and therefore had considerable uncertainties. These were therefore rejected as suitable targets for modeling. Six daily profiles (Dec 8, 10, 12, 13, 14, 17) were selected for our analysis spanning latitudes from 23°–60°S, local times ~08–09 h, and solar zenith angles of ~78–89°.

[11] The ionosphere in the southern hemisphere of Mars does exhibit longitude effects due to the presence of crustal magnetic fields, and particularly so near 180° longitude. This alerts us to the fact that care must be taken in selecting MEX profiles that comprise an acceptable data set for comparisons with results from the northern hemisphere where any effects related to crustal-**B** influenced processes can be assumed to be minor. *Withers et al.* [2005] examined a number of MGS profiles from the southern hemisphere and found that they were more irregular in shape, with localized "bite-outs" and "bumps" when observed above regions known to have strong crustal **B**-fields. In that limited set of examples, the irregularities appeared as features upon otherwise smoothly varying N_e (h) profiles. This suggested that photochemistry was still the dominant process, with perhaps particle precipitation and/or plasma instabilities creating superimposed additions or depletions of plasma. Further effects of magnetic fields on ionospheric properties are summarized by *Withers* [2009]. The six days of MEX observations available for this study happened to have $N_e(h)$ profiles mostly in areas with strong **B**-fields. These provide the opportunity to explore physical mechanisms operating on Mars in areas with (MEX) and without (MGS) crustal fields.

3. Observations

3.1. Presentation of Data

[12] In Figure 1 we show examples of MGS and MEX observations on single days. The dates are selected to

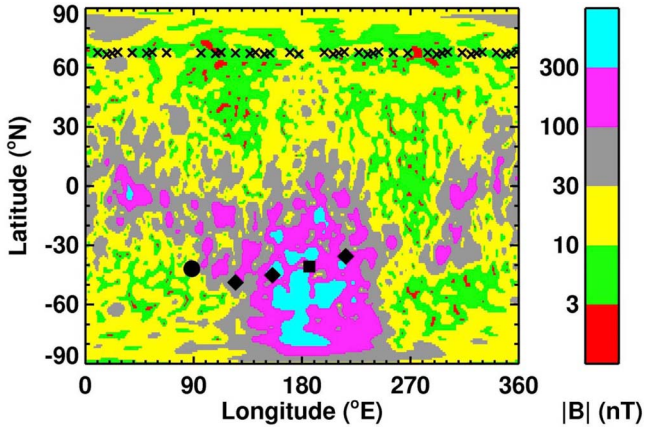

Figure 2. A map showing the magnetic field strength at 150 km predicted by a model of the crustal magnetic fields [*Arkani-Hamed*, 2004]. The diamonds show the locations of the five individual $N_e(h)$ profiles obtained by the MEX radio occultation experiment on December 10, 13 and 14, 2004. There are two profiles observed on December 12, 2004. One of these (solid square) occurs in a region of strong crustal B-field, while the other (solid circle) does not. In the northern hemisphere, MGS observations on these four days had 40 points of observations versus longitude. These are shown by crosses, and none falls in regions of strong crustal-**B** fields.

exhibit cases of maximum and minimum variability, a useful dichotomy for judging the nature of a daily mean obtained by averaging longitudinally distributed data (to be compared later with our model output). Figure 1a shows the 8 MGS profiles obtained on 29 December 2004, a day of minimal variability. The M1 and M2-layers are clearly visible. In Figure 1b, 9 MGS profiles from 26 December 2004 are shown, a day of more pronounced variability, but with comparable mean values for the M1 and M2-layers shown in Figure 1a. The average heights of the layer peak densities are also comparable in both panels. For MEX, Figure 1c shows the two electron density profiles recorded on 12 December 2004—an example of both individual profiles, as well as longitude variability for the only daytime period when more than one MEX profile was available. Both profiles show acceptable agreement for the M1-layers and in the topside shapes up to ~180 km. For the M2-layer, the profile on the right shows some small-scale irregularity just above the height of the main peak and a somewhat higher peak density (but no more so than in the maximum and minimum cases shown in Figure 1b for MGS data). The profile shown by a dotted line is outside regions of strong **B** while the one given by the solid line is within such a region. In contrast to the *Bougher et al.* [2001] results from MGS observations in the northern hemisphere, there are no known systematic variations in the heights of the M1 and M2 layers in the southern hemisphere. Thus, we averaged observations on this only day with two MEX profiles. The resultant profile (thick dashed line) captures the essential features of distinct M1 and M2-layers. We will use this daily mean (together with the other single profiles per day) for comparisons with photochemistry, and comment later on the possible significance of other processes that might lead to distinction between the two profiles on that day. In summary, Figure 1 demonstrates that the daily mean curves from MGS and MEX are of sufficient quality to support the modeling studies intended.

3.2. Further Considerations About Observations Near Crustal Magnetic Fields

[13] As discussed above, the MGS data sets pertain to locations in the northern hemisphere where crustal magnetic fields are negligible, while the opposite case occurred for the MEX observations in the southern hemisphere. In Figure 2, we show the locations on four specific days of the MGS and MEX observation points with respect to the patterns of magnetic fields at Mars. In the northern hemisphere, the MGS observations on December 10, 12, 13 and 14 had multiple locations, with 8, 10, 13, and 9 profiles available, respectively, to form the daily averages. Their individual locations are shown by the large X notations. Clearly, there is little concern when using them to form daily averages since they have a robust distribution over longitudes that do not contain crustal **B**-fields. For the MEX observations in the southern hemisphere, single profiles were obtained on December 10, 13 and 14; their locations are shown by the black diamonds and all are in areas of strong magnetic fields. The two profiles obtained on 12 December fall within a strong **B**-field (solid square) and a region of negligible crustal-**B** values (solid circle). These latter two profiles are the ones shown in Figure 1c. Given that our modeling will address the average of four days of profiles from MGS and MEX, concern that the daily average from MEX had one of five profiles away from strong **B**-fields is minor. Yet, there are some morphology aspects to note in Figure 1c. Starting on the bottom side, there are no significant differences in the M1-layer, either in altitude or magnitude. This is to be expected if that layer is produced only by persistent soft X-rays of solar origin on that day. The low-altitude agreement of both MEX profiles also implies that there were no additional energetic particle precipitation-induced sources of plasma at the strong-**B** locations at these times. For the M2-layer, the magnitudes of the two peak electron densities from MEX on 12 December differ by ~20% from their mean. This is not a strong difference (see MGS data in Figures 1a and 1b), but the larger value is indeed for the profile within a **B**-field. For topside ionosphere heights, the profiles are in close agreement, suggesting that in situ soft energetic particle (~100 eV) precipitation (effects that would augment solar production of plasma [*Schunk and Nagy*, 2009]) are not causing localized profile changes above the crustal-**B** location at this time.

[14] Given that the $N_e(h)$ profiles in Figure 1c differ only at the peak, and that such peak density variability is within normal limits, there is no conclusive evidence to suggest that processes other than chemistry were operative to any degree of concern. Moreover, the types of ionospheric irregularities known to exist over crustal-**B** areas, so-called electron density "bumps and bite-outs" [*Withers et al.*, 2005], are most often found in the topside; there is only minor evidence of such effects in Figure 1c.

[15] Our conclusions are twofold: First, for the photochemical processes central to this study, the average MEX profile on 12 December is representative of the morphology found on the other three days, and thus no fundamental differences exist between above-**B** versus without-**B** profiles

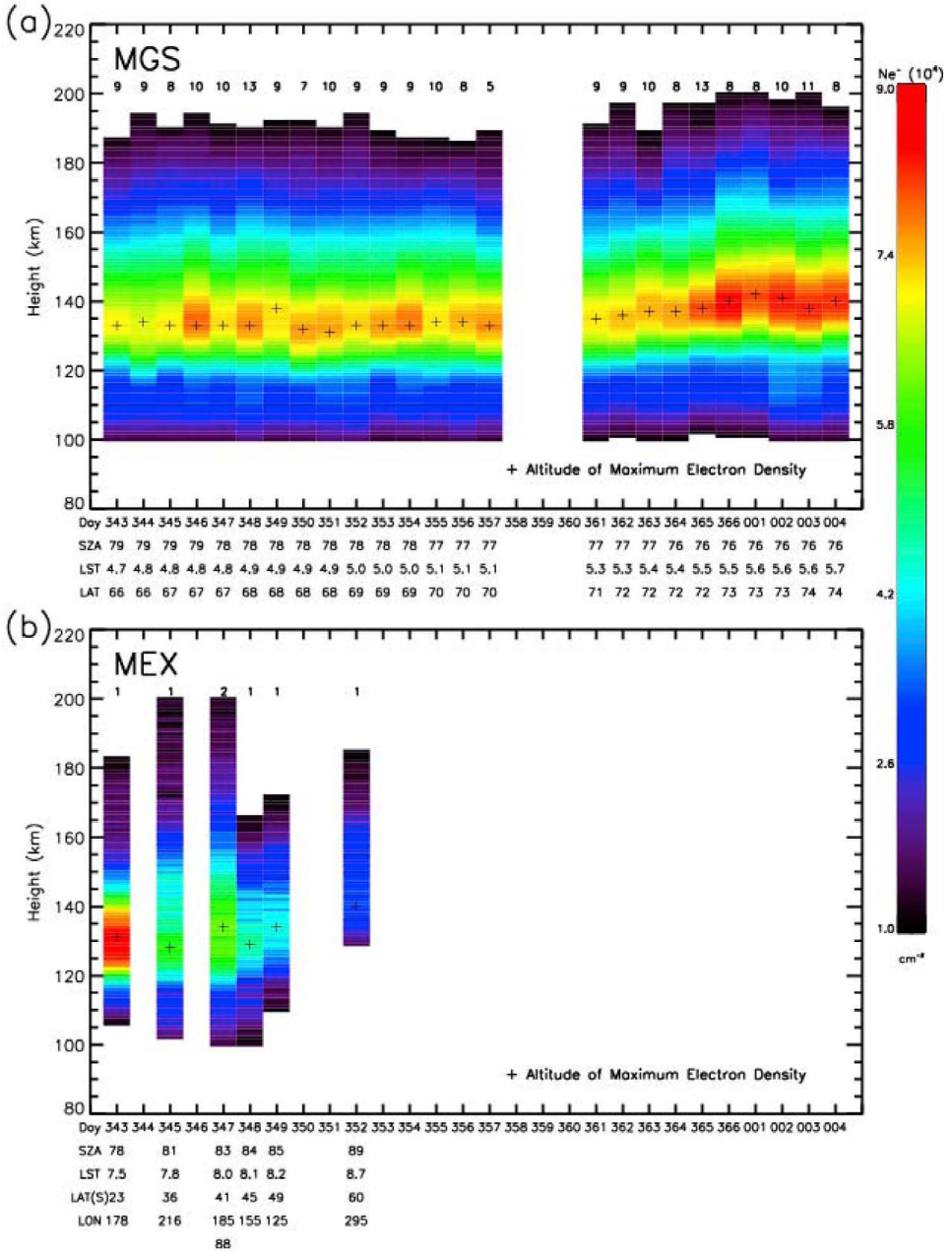

Figure 3. Time histories of the daily mean electron density profiles from (a) MGS and (b) MEX during the period 8 December–4 January 2005, day numbers 343–004, Ls = 125–139. Figure 5 gives solar activity during this period. The electron density values are portrayed using the same color coding. Below each data set are the daily values of latitude (° North), local time (hrs) and solar zenith angle (°). At the top, the number of individual observed profiles used to make the daily averages is displayed. The four days (#345, 347, 348, and 349), corresponding to December 10, 12, 13, and 14, represent a set of stable conditions with observations by both the MGS and MEX satellites. Note that day 347 is the only day when two MEX profiles are used to create a daily average, and that separate longitudes are given.

in this study. Second, additional observations and modeling are needed to understand the multiple influences that the crustal-**B** fields can exert on ambient plasma production and loss, on plasma instabilities and upon plasma dynamics in such regions. Given that the spatial morphology of the crustal **B**-fields are highly structured in both the meridional and zonal directions, 2 or 3- dimensional models are needed to handle plasma processes correctly in such locations.

3.3. The Full MGS and MEX Data Sets

[16] In Figure 3, we show the time history of the daily profiles for MGS (Figure 3a) and MEX (Figure 3b) selected from this overlap period. Below each panel are multiple

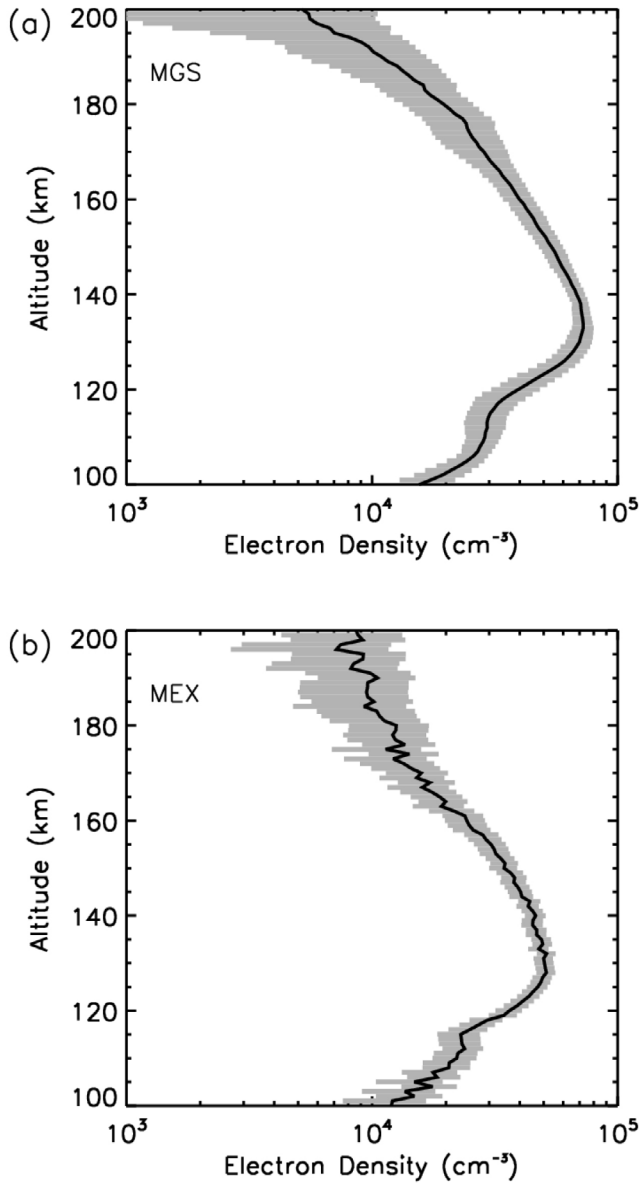

Figure 4. Average of all electron density profiles observed on December 10, 12, 13 and 14, 2004, used to define the modeling goals: (a) from 40 MGS profiles, with shading for standard deviations, and (b) from 5 MEX profiles, with shading to portray average uncertainties in observations.

scales to indicate latitudes, longitudes, local times, and solar zenith angles. This particular format of using a color bar for the magnitudes of electron density does not portray the M1-layer (or ledge) well. We will use line-profiles in the modeling section below to study these features more closely. In examining these data sets, note that the period in mid-December 2004 (DOY 343–357) (Figure 3a, left) represents a relatively stable set of conditions for profiles observed by MGS. At later dates in Figure 3a, however, there is a somewhat separate group of profiles (DOY 365 to DOY 004 in 2005) with higher electron densities. There are no simultaneous MEX data for these days and thus the two subsets of MGS observations will be used for assessing variability internal to the MGS database.

[17] For the MEX data during this period (Figure 3b), there are also two subsets to notice. The first and sixth days (December 8 and 17, DOY 343 and 352) have latitudes significantly equator-ward and pole-ward, respectively, with correspondingly lower and higher solar zenith angles, than occurred for the central four days. The four central days of MEX data offer a self-consistent set that have an average latitude of 44°S and an average local time of ~08:00, corresponding to an average solar zenith angle of 83°. Fortunately, MGS data also were available on all six of those MEX days, and the four central ones have profiles at an average latitude of 67°N and an average local time ~05:00, corresponding to an average solar zenith angle of 78°. The mean of all of the MGS profiles on these four days (together with standard deviation versus height) are shown in Figure 4a. The mean of the four daily MEX profiles are shown in Figure 4b, also with their average observed uncertainty levels versus height in Figure 4b. These mean curves in Figures 4a and 4b constitute the observational data set that we will use as the modeling targets for our same-day modeling efforts.

[18] To place these data sets into the context of orbital locations and solar conditions, we show in Figure 5a the positions of Earth and Mars during this 28 day period. This time span corresponds, approximately, to a solar rotation. Figure 5b shows the indices commonly used to characterize solar flux (F10.7) and geomagnetic activity (Ap) at Earth. The mean F10.7 level of ~90 ± 5 units corresponds to low solar activity with no active regions during this period. This provides confidence that solar observations made from Earth pertain to Mars as well (i.e., we will not attempt "solar rotation" corrections to estimate different irradiances at Mars) since the uncertainties in doing so probably exceed the variability in solar output during this period of solar quiescence. Geomagnetic activity was generally low at Earth, except for the last few days. Given that our core period of interest occurred earlier, we assume that changes in the solar wind conditions impinging upon the planet are not a significant source of variability.

4. Model

4.1. Model Description

[19] To model the ionosphere at Mars in a way that will allow for the flexible exploration of parameter space options and their resultant effects, it is often useful to create a 1-dimensional (vertical) model. Indeed, as reviewed in the Introduction, all of our basic knowledge of the Martian ionosphere rests, arguably, upon simulations and insights from 1-D models (e.g., *Nier and McElroy* [1976], *Chen et al.* [1978], *Fox and Dalgarno* [1979], *Singh and Prasad* [1983], *Nair et al.* [1994], *Krasnopolsky* [2002], *Haider et al.* [2010], and many others). In addition, there currently exist several 3-dimensional models for Mars that are comprehensive general circulation models (GCMs) of the coupled neutral and ionized components of the upper atmosphere [see, e.g., *Bougher et al.*, 2009]. It is often difficult to conduct a broad series of "simulation experiments" to illuminate effects produced by individual aeronomic processes in fully coupled GCMs [*Bougher et al.*, 2009] and MHD codes [*Ledvina et al.*, 2008]. In addition, such models often have a high demand for computer resources. Thus, in this

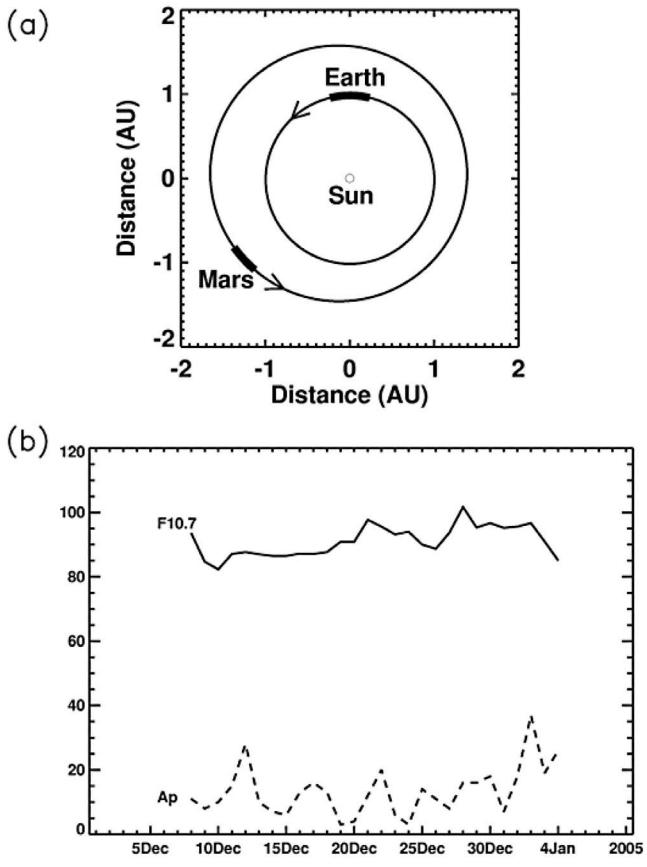

Figure 5. (a) The orbital configuration of Earth and Mars during the period 8 December 2004–4 January 2005. (b) Daily values of the solar flux index F10.7 and the geomagnetic activity Ap, both observed from Earth during this period.

study we concentrate on exploring several physical processes using the 1-dimensional simulation approach described by *Martinis et al.* [2003].

[20] The *Martinis et al.* [2003] 1-D model code used a neutral atmosphere of ten species (CO_2, N_2, O, O_2, CO, Ar, NO, He, H_2 and H) spanning the height range 80–400 km and corresponded to solar maximum conditions. The solar irradiance (photon flux versus wavelength) used to compute the diurnal production of five species (O_2^+, CO_2^+, O^+, N_2^+ and NO^+, and their associated electrons) came from the SOLAR2000 v1.24 model of *Tobiska* [2004]. This ion population was transformed by several ion-neutral chemical reactions, and the electrons and ions chemically recombined in a series of reactions that led back to neutrals. The electron density was formed by summing all ions present at a given time and altitude to yield the electron density profile, $N_e(h)$.

[21] The model used for this study adapts the core photochemistry within the *Martinis et al.* [2003] framework (see Table 1a) and adds multispecies plasma diffusion. We also update the solar irradiance model from version 1.24 to version 2.27 that covers the spectrum from λ = 1.86 to 105.0 nm. We use the version of SOLAR2000 that gives irradiance values in a combination of 39 wavelength bins that comprise small bands and spectral lines. For the neutral atmosphere, we now use the European Mars Climate Data Base (MCDB) model [*Lewis et al.*, 1999; *Forget et al.*, 1999] described further in Section 4.2 that includes the five dominant species (CO_2, N_2, O, CO and H_2). There are no magnetic field effects in the model (a condition we will discuss more fully in Section 6.2), and thus plasma diffusion is assumed to be purely vertical. Only ion-neutral collisions are assumed for plasma diffusion (i.e., no ion-ion or electron-ion collisions), and no vertical winds or electric fields are considered.

[22] In Figure 6 we present two aspects of solar irradiance. In Figure 6a there are 28 daily values of photon flux in each of the 39 wavelength bins, corresponding to the MGS/MEX overlap dates of 8 December 2004 to 4 January 2005. In Figure 6b the variability present in each wavelength bin is portrayed using the standard deviation, σ(%), about the mean of each bin in Figure 6a. These latter values will be used to explore the causes of observed variability. Finally, all cross-sections for absorption and ionization, appropriate for the same 39 wavelength bins, have been taken from *Schunk and Nagy* [2009] for bins #3–39; those for bins #1 and #2 were computed independently from *Verner and Yakovlev* [1995] and *Verner et al.* [1996] and are shown in Table 1b.

[23] Secondary ionization (the creation of multiple ion-electron pairs from single photon absorption) was handled by *Martinis et al.* [2003] by applying an altitude-dependent multiplicative factor to the primary photo-ionization rate. That parameterization factor was based on the results of *Fox et al.* [1996], as we do initially here. Secondary ionization is a poorly constrained process at Mars in that neither daily measurements of the sun's soft X-rays nor daily observations of the M1-layer electron densities are available at Mars.

[24] Computationally, we calculate a set of plasma, photochemical and diffusion parameters used by the model (scale heights for plasma and neutrals, reaction rates, ion-neutral

Table 1a. Model Parameters: Photo-Ionization and Chemistry Included in the Model

	Reaction	Rate Constant (cm^3/s) [*Schunk and Nagy*, 2000]
(a)	$CO_2 + h\nu \rightarrow CO_2^+ + e^-$	
(b)	$O + h\nu \rightarrow O^+ + e^-$	
(c)	$N_2 + h\nu \rightarrow N_2^+ + e^-$	
1	$CO_2^+ + O \rightarrow O^+ + CO_2$	$k_1 = 9.6 \times 10^{-11}$
2	$CO_2^+ + O \rightarrow O_2^+ + CO$	$k_2 = 1.6 \times 10^{-10}$
3	$N_2^+ + CO_2 \rightarrow CO_2^+ + N_2$	$k_3 = 8.0 \times 10^{-10}$
4	$N_2^+ + O \rightarrow O^+ + N_2$	$k_4 = 9.8 \times 10^{-12}$
5	$N_2^+ + O \rightarrow NO^+ + N$	$k_5 = 1.3 \times 10^{-10}$
6	$O^+ + N_2 \rightarrow NO^+ + N$	$k_6 = 1.2 \times 10^{-12}$
7	$O^+ + CO_2 \rightarrow O_2^+ + CO$	$k_7 = 1.1 \times 10^{-9}$
8[a]	$CO_2^+ + e^- \rightarrow CO + O$	$\alpha_1 = 3.1 \times 10^{-7} \times (\frac{300K}{T_e})^{0.5}$
9	$N_2^+ + e^- \rightarrow N + N$	$\alpha_2 = 2.2 \times 10^{-7} \times (\frac{300K}{T_e})^{0.39}$
10	$O_2^+ + e^- \rightarrow O + O$	$\alpha_3 = \begin{cases} 1.95 \times 10^{-7} \times \left(\frac{300K}{T_e}\right)^{0.7} & for\ T_e < 1200K \\ 7.38 \times 10^{-8} \times \left(\frac{1200K}{T_e}\right)^{0.56} & for\ T_e > 1200K \end{cases}$
11	$NO^+ + e^- \rightarrow N + O$	$\alpha_4 = 4.0 \times 10^{-7} \times (\frac{300K}{T_e})^{0.5}$

[a]Using the more recently proposed values from *Schunk and Nagy* [2009] affected the modeled electron density at the peak by ~10%, which is less than the variability shown in the data.

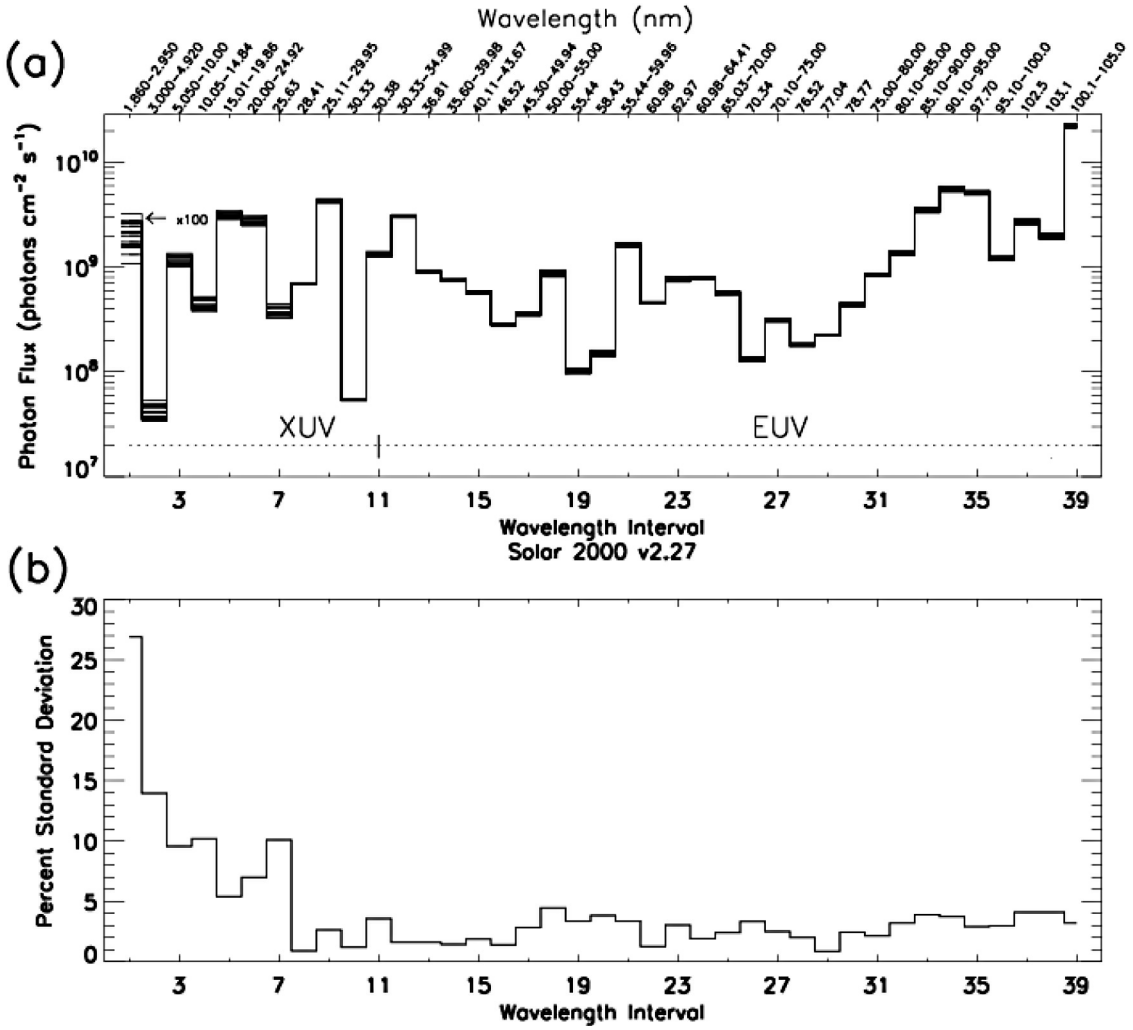

Figure 6. (a) The solar irradiance values from the SOLAR2000–2.27 model for the 28 days from 8 December 2004–4 January 2005. Notice that wavelength bin #1 has been multiplied by 100 for display purposes. This and other low wavelength bins (soft x-rays) pertain to the photon fluxes most responsible for the M1-layer at Mars. Wavelength bin #11 pertains to the Helium 30.4 nm emission in the EUV that is a strong source for the M2-layer. (b) The variability of irradiance for each wavelength bin using the standard deviation about the mean, expressed in percent, to portray solar variability patterns during the period under study.

collision frequencies, ambipolar diffusion coefficients, diffusion timescales, critical time steps for computational stability, and optical depths using a Chapman grazing incidence integral [*Smith and Smith*, 1972]). We then apply a photochemical model to track the ion densities of each ion species, as is described by *Martinis et al.* [2003] and summarized below:

$$N = N_0 e^{-Rt} + \frac{P}{R}\left(1 - e^{-Rt}\right) \quad (1)$$

where

N = new ion density of a constituent;
N_0 = original ion density of a constituent;
R = chemical loss rate;
t = model time increment;
P = total production rate = production of ions due to primary and secondary ionization, as well as via chemical processes (reaction of neutrals with ions).

[25] After each time step of photo-chemistry we compute the diffusion of ions using the same time step. If either chemistry or diffusion changes the number density of a species within a cell by more than a pre-set percentage, the time step for both processes is halved until the criteria is satisfied. Given the small time steps to be used, the alternate updating of chemistry and dynamics presents no concerns about the overall stability of results obtained. This technique was developed for a one-dimensional model for Saturn's ionosphere [*Moore et al.*, 2008, 2009] that was validated via agreement with a fully coupled three-dimensional thermosphere global circulation model [*Müller-Wodarg et al.*,

Table 1b. Model Parameters: Cross Sections for Absorption and Ionization for Solar Irradiance Bins Not Listed in Work by *Schunk and Nagy* [2009]

Bin[a]	N_2	N_2^+	O	O^+	CO_2	CO_2^+	CO	CO^+	H_2	H_2^+
1	0.8235	0.8235	0.0313	0.0313	0.3199	0.3199	0.2886	0.2886	0.0003	0.0003
2	0.1392	0.1392	0.1200	0.1200	1.0793	1.0793	0.9592	0.9592	0.0013	0.0013

[a]Units are in Mb (10^{-18} cm^2). Cross sections for a molecular ion represent the sum of all ionization cross sections of the neutral species. For these high energy wavelength bins (~18–50 Å) the cross sections for absorption and ionization are identical.

2006], subsequently updated to incorporate ionospheric processes (I. Müller-Wodarg, private communication, 2008). The specific formulation is as follows:

$$N = N_0\left(1 - \frac{V_{ion}t}{d}\right) \tag{2}$$

where t is model time increment, d is the altitude spacing between adjacent grid points, and V_{ion} is the ion diffusion velocity given by:

$$V_{ion} = -D_a\left[\frac{1}{H_P} + \frac{T_i}{T_P}\frac{d(\log N_i)}{dz} + \frac{T_e}{T_P}\frac{d(\log N_e)}{dz} + \frac{d(\log T_P)}{dz}\right] \tag{3}$$

from equation 19.60 of *Banks and Kockarts* [1973], with

$$D_a = \text{the ambipolar diffusion coefficient} = \frac{T_P}{T_i}\frac{(kT_i/m_i)}{\sum_n \nu_{in}}, \tag{4}$$

$H_P = \frac{kT_P}{m_i g}$;
T_i = ion temperature;
T_e = electron temperature;
T_P = plasma temperature = $T_i + T_e$;
N_i = ion density;
N_e = electron density;
k = the Boltzmann constant;
m_i = ion mass;
g = gravity;
ν_{in} = ion-neutral collision frequency.

[26] For each ion species, the upper boundary condition applied is that the individual densities decrease exponentially using their fixed plasma scale heights at the grid point below 400 km. Since diffusion is negligible at the lower boundary, i.e., stationary photo-chemistry dominates, no additional boundary conditions were needed there. The model is run for ~2 days of model time to generate a stable ionosphere. The time steps start with very small values ($\ll$1 s) and evolve dynamically with the ionosphere depending on the percent change of ion and electron densities from the previous time step. Current model settings restrict this change to be <2% from one time step (typically 45 s) to the next.

[27] For height resolution, we use 70 cells spanning the altitude range from 80–400 km. The cells span 1 km at the lower boundary and increase to 20 km at the top boundary.

4.2. Model Results

[28] Our approach to modeling this period of MGS-MEX overlapping data sets is to explore the range of parameters that contribute to the absolute magnitudes and heights of the two main layers (M1 and M2) as found in observed $N_e(h)$ profiles. Our primary set of simulations will deal with attempts to model the mean behavior of the profiles in Figure 4, that is, the subset of least variable days from MEX and their MGS counterparts. We will run the model separately for each of those four days and form their average $N_e(h)$ to compare with Figure 4. Based on those results, we will then return to the overall variability pattern spanning the full set of overlapping data shown in Figure 3.

[29] The first step is to select the neutral atmospheres for the MGS and MEX observing locations in each hemisphere. A recent treatment of the full 3-dimensional neutral atmosphere at Mars appears in work by *Bougher et al.* [2009]. Given our goal of conducting many simulation experiments using several parameterization schemes for key processes, we needed to identify a flexible way to obtain neutral atmospheres for our 1-dimension calculations. This is done routinely for ionospheric modeling at Earth using the NRL MSIS model of *Picone et al.* [2002]. Input parameters are latitude and longitude of the site in question, plus the date and time in order to obtain the appropriate seasonal, solar cycle and geomagnetic conditions. The output includes number density versus height of each neutral species, plus the neutral temperature profile. For Mars, there is a less-well validated empirical model, but one that approaches the philosophy behind the terrestrial MSIS model, i.e., a readily available way to get upper atmosphere neutral number density and temperature profiles for a specified site, at a specific time, and for a selection of dust levels in the lower atmosphere: the Mars Climate Data Base (MCDB). The MCDB is a statistically compiled database that includes simulations from the General Circulation Models of two independent European groups, and has been validated with observational data. The output of the MCDB is publically available online (http://www-mars.lmd.jussieu.fr/) and gives the total mass density at a lower boundary of 80 km, together with the mean molecular mass, mixing ratios by number density of five species and neutral temperature. There are also density profiles of each neutral species and a temperature profile up to an altitude of ~230 km. Our needs are to cover altitudes 80–400 km, and thus a specialized use of the MCDB was developed, as described next.

[30] To access the MCDB for this study, we used the orbital position of Mars (its solar Longitude, Ls) for the period of observations, and selected the low dust level case. In anticipation of having to adjust the MCDB output to match simulations with data, we decided to use the most basic output from the MCDB, namely, the values of total density and species volume mixing ratios at the lower boundaries (~80 km) for the MGS and MEX data locations for the four common days, together with their exospheric

Table 2. Mars Climate Data Base Parameters at 80 km

Quantity	MGS Site	MEX Site
Atmospheric Density (kg m^{-3})	1.754×10^{-12}	1.376×10^{-12}
Reduced Atmospheric Density (kg m^{-3})	7.893×10^{-13}	6.192×10^{-13}
Reduced Number Density (# m^{-3})	1.09×10^{13}	8.54×10^{13}
Exospheric Temperature[a] (K)	204.3	189.5
Mixing Ratio of O (by Volume)	0.003893	0.00217
Mixing Ratio of CO (by Volume)	0.005588	0.003252
Mixing Ratio of CO_2 (by Volume)	0.9443	0.9472
Mixing Ratio of N_2 (by Volume)	0.02818	0.0289
Mixing Ratio of H_2 (by Volume)	1.617×10^{-5}	1.658×10^{-5}

[a]Exospheric temperature is taken at 230 km.

temperatures (at ~230 km). With the concentrations for O, CO_2, N_2, CO and H_2 specified at 80 km, we then calculated their altitude distributions to 400 km under the influence of eddy and molecular diffusion as formulated by *Krasnopolsky* [2002] with the binary diffusion coefficients of *Chamberlain and Hunten* [1987]. The specific equations used are as follows:

$$\Phi_i = -(K + D_i)\frac{dn_i}{dz} - n_i\left[K\left(\frac{mg}{kT} + \frac{1}{T}\frac{dT}{dz}\right) + D_i\left(\frac{m_i g}{kT} + \frac{1+\beta}{T}\frac{dT}{dz}\right)\right] \quad (5)$$

where Φ_i is the flux of a neutral species, K and D are the mixing and binary diffusion coefficients given below, n is the number density, m is the mean molecular mass, m_i is the neutral species mass, g, k and T are the gravitational acceleration, Boltzmann's constant and neutral temperature, respectively. β is a thermal diffusion factor that is −0.25 for H_2, and 0 for the rest of our neutral species.

[31] K is a mixing coefficient in $cm^2 s^{-1}$ that includes effects of eddy diffusion and large-scale winds and is given by:

$$K(z) = 1.2 \times 10^{12}\sqrt{\frac{T_\infty}{n(z)}} \quad (6)$$

where T_∞ is the exospheric temperature in Kelvin, and n(z) is the neutral density in cm^{-3}.

[32] The binary diffusion coefficient D_i of gas i diffusing through other gasses is given as [*Colegrove et al.*, 1966]:

$$D_i = \frac{\sum_j n_j}{\sum_{j\neq i}\frac{n_j}{D_{ij}}} \quad (7)$$

where n_j is the gas number density and D_{ij} is the diffusion coefficient of gas i through another gas j. Using the hard-sphere approximation [*Chamberlain and Hunten*, 1987]:

$$D_{ij} = \frac{1}{n_i} * \frac{3}{4\pi(\sigma_i + \sigma_j)^2} * \left[\frac{2\pi kT(m_i + m_j)}{m_i m_j}\right]^{1/2} \quad (8)$$

where σ_i and σ_j are the collision diameters, m_i and m_j are masses of gases i and j respectively. k is the Boltzmann's constant and T is temperature.

[33] We also decided to use Krasnopolsky's parameterization of atmospheric temperature versus height keyed to the exospheric temperature provided by the MCDB. The Krasnopolsky formula provides an analytical expression for T_n(K, h) that is convenient for later parameterization developed to relate plasma temperatures (T_e and T_i) to the neutral temperature profile.

$$T(z) = T_\infty - (T_\infty - 125K)e^{\left(-\frac{(z-90km)^2}{11.4T_\infty}\right)} \quad (9)$$

where T(z) is the neutral temperature in Kelvin at an altitude z in km, T_∞ is the exospheric temperature in Kelvin taken from the Mars Climate Data Base.

[34] Finally, we found that it was not necessary to change the MCDB neutral profiles each day, i.e., they were virtually identical for the four days in question at each hemispheric site.

[35] Our simulations are done for the altitude range 80–400 km. The 400 km height is well above the domain where MGS (but not MEX) have observations, but altitudes up to 400 km are needed for correct modeling of the attenuation of solar photons by the neutral atmosphere. Moreover, it is useful to have such a broad range in order to explore where regions are dominated by chemistry, dynamics, or both. As will be shown in Section 6, model runs were made with photo-chemistry-only versus runs with photo-chemistry-plus-plasma diffusion. Several important conclusions came from these results. First is that diffusion becomes important at heights above ~170 km, well above the M1 and M2-layers of prime interest (i.e., for which both MGS and MEX data exist). This allows us to explore parameters controlling key processes of the two main layers by using the photo-chemical-only part of the code, thereby minimizing demands on computer simulation time. Second, since diffusion is not of crucial importance for the M2 peak (well below 200 km), our modeling assumption of no magnetic fields (and thus no field-aligned diffusion versus vertical diffusion) is clearly not a major concern. Thus, in subsequent figures of this and the following section, we will portray results only within the 80–200 km range, i.e., a subset of the full 80–400 km simulation. Consistent with this limitation is the fact that the solar wind and its magnetic field can penetrate down to heights between 300 and 400 km, and such "ionopause interactions" [*Brain et al.*, 2003] are not in the model. Our main goal, once again, is to achieve success with the M1 and M2 layers under varied but highly constrained conditions, and to leave topside ionosphere modeling for later developments. We return to the topic of additional chemical and dynamical processes acting in the topside ionosphere in Section 6.

4.3. Adjustments to the Model

[36] We conducted a series of three computer simulation experiments that involved (1) changes in the neutral atmosphere, (2) changes in electron temperature, and (3) changes in the efficiency of photo-electrons producing secondary ionization. We now describe each of these.

4.3.1. Effects of the Neutral Atmosphere

[37] The first disagreements to address between observations and model are the differences between the peak heights of the M2-layer and, to a lesser extent, those for the M1-layer. The issue is the attenuation of ionizing radiation

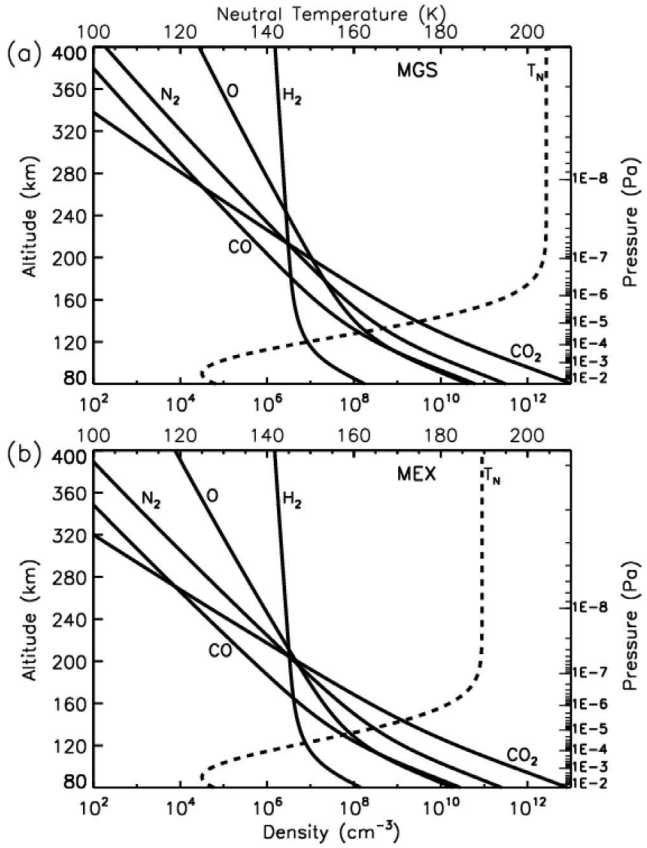

Figure 7. The neutral upper atmospheres derived from the Mars Climate Data Base (MCDB) appropriate for the hemispheres and times of the observations: (a) for the northern-summer (MGS) site and (b) for the southern-winter MEX site (see text).

through the neutral atmosphere. The M1 and M2-layers occur near unity optical depth for their respective wavelengths of importance. We found (via trial and error) that the total number density at the lower boundary (80 km) as obtained from the initial MCDB atmosphere had to be lowered. A single multiplication factor of 0.45 was used for both the MGS and MEX sites. Modified neutral atmospheres were calculated using these reduced base densities (see Table 2) by setting the flux Φ in equation (5) to zero and integrating upwards from 80 km. The resultant atmospheres are the ones shown in Figure 7. The electron density profiles from those atmospheres are shown by the dotted-lines in Figure 8. The black lines with shading give observations and uncertainties; the dashed lines give the computed $N_e(h)$ profiles from the un-modified MCDB atmosphere, while those with dotted lines come from the tuned atmosphere. In both cases, the modified atmospheres achieved the desired reduction in the height of peak density. Note that we decided upon a neutral atmosphere adjustment that resulted in the height of the M2 peak density to be slightly lower than observed because we knew from subsequent model modifications that electron temperature effects (treated next) would move the peak height upward.

4.3.2. Effects of Electron Temperature

[38] As shown in Tables 1a and 1b, the dissociative recombination of molecular ions and electrons in the Martian ionosphere is the final step in the overall photo-chemical system. Such plasma loss reactions proceed faster if the electron gas is cool, and thus the reaction rates for chemical loss show an inverse dependence on the electron temperature (T_e). For an ionospheric layer in photo-chemical equilibrium, the resultant electron density would then increase as the electron temperature does (i.e., reducing loss for the same amount of production). Equation 13.7 of *Schunk and Nagy* [2009] shows this to be a weak dependence [$N_e \approx (T_e)^{0.35}$ for dissociative recombination of O_2^+], yet for the temperatures of relevance in the Martian ionospheric layers, an enhancement of a few hundred degrees K can have noticeable effects. Moreover, plasma temperatures (T_i and T_e) and their gradients can affect plasma diffusion, as indicated in equation (3).

[39] Within the dense atmosphere that defines the dominance of photochemistry in the M1-layer, collision processes are so frequent that neutrals, ions and electrons are expected to have similar temperatures. The situation of $T_n = T_i = T_e$ is far less likely for the higher altitude (M2) layer. The only in situ observations to date (from Viking landings) confirm that the plasma temperatures deviate from the neutral temperatures [*Hanson et al.*, 1977; *Hanson and Mantas*, 1988]. Initial modeling studies showed that the

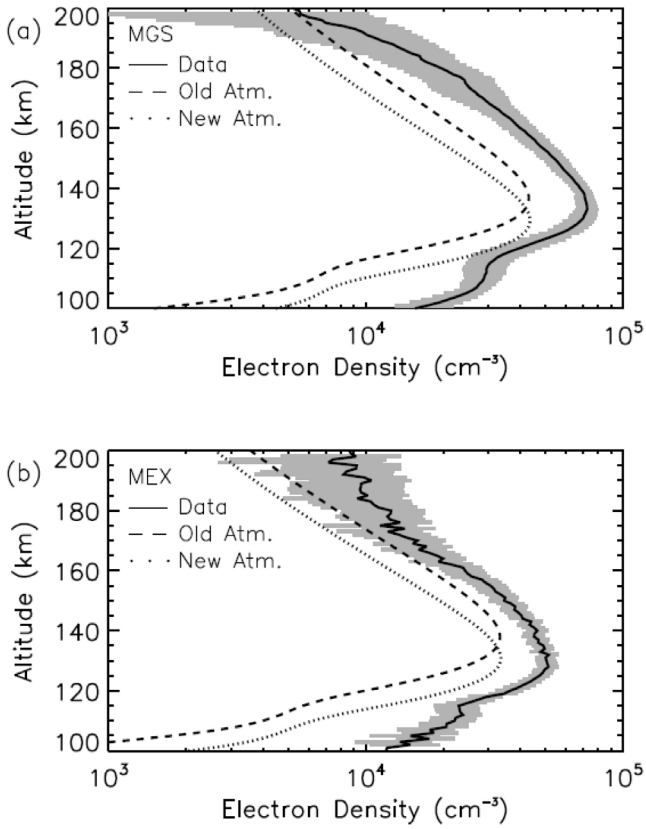

Figure 8. Results from the neutral atmosphere adjustment study. In each panel, the solid line with shading gives the observed pattern of electron density profile with uncertainty levels. The dashed-lines give the model results using the original MCDB neutral atmospheres, and the dotted-line gives results from the adjusted atmosphere as shown in Figure 7. (a) MGS and (b) MEX comparisons.

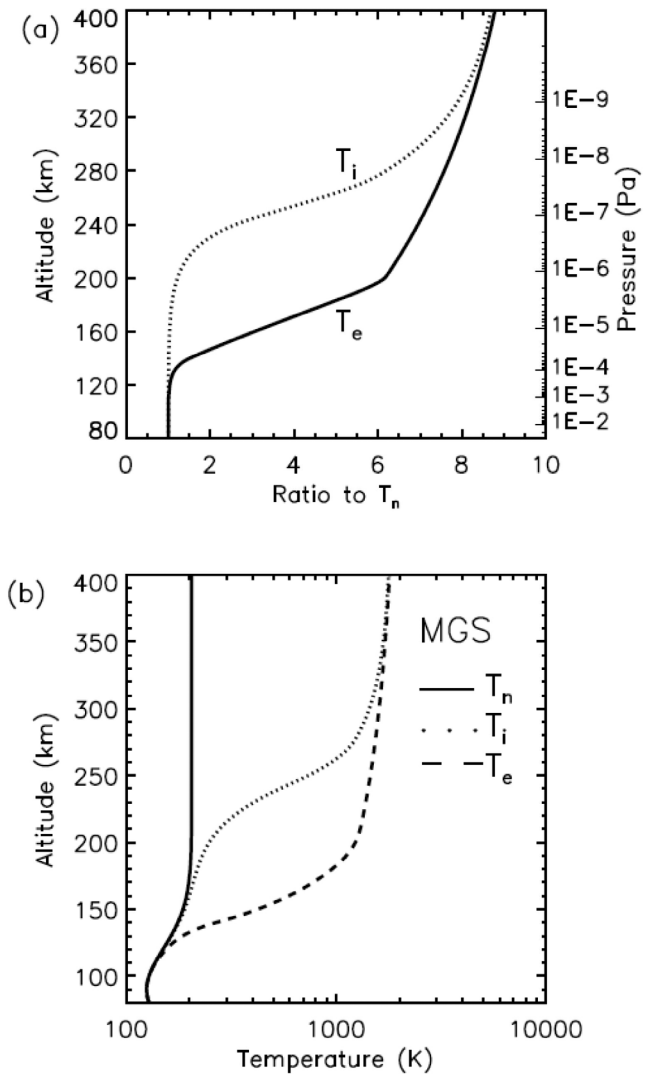

Figure 9. The parameterization scheme for plasma temperatures adopted in the model. (a) The curves give the multiplicative factors applied to the neutral atmosphere temperature (T_n) to estimate the electron temperature (T_e) and ion temperature (T_i). (b) The resultant profiles of T_n, T_e and T_i shown with an altitude scale for the MGS site. The pressure level scale (right axis) in Figure 9a is used to adapt these parameterizations to the different atmosphere at the MEX observing site (see text).

electron gas starts to diverge from thermal equilibrium with ions and neutrals near 130 km [*Chen et al.*, 1978; *Rohrbaugh et al.*, 1979]. Follow-up work by *Fox et al.* [1996], *Choi et al.* [1998], and *Fox and Yeager* [2006] showed that that the plasma temperature patterns are of fundamental importance for the M2-layer. This could be even more crucial at dawn, though that possibility has not been examined at Mars. For example, *Safaeinili et al.* [2007] observed larger electron densities in post-sunrise MARSIS observations than in pre-sunset observations at identical solar zenith angles, which is consistent with high post-sunrise electron temperatures. For the terrestrial and Saturnian cases, photons at sunrise produce a rarified, hot electron gas that takes a while (~hours) to lose energy to the ions and neutrals (see examples of this "post-sunrise effect" in T_e at Earth in the book by *Schunk and Nagy* [2009] and at Saturn in the work by *Moore et al.* [2008]).

[40] A first principles model of thermal balance in a planetary ionosphere is a significant task, as reviewed recently for Saturn by *Moore et al.* [2008]. To have a more flexible method of estimating electron and ion temperatures in simple models, we take the approach of developing a parameterization scheme that relates T_e and T_i to the temperature of the neutral atmosphere (T_n). We based this on the Viking T_e and T_i measurements, which have T_e asymptotically approaching an exospheric value above 200 km, $T_i = T_n$ below 170 km, and T_i approaching T_e above 300 km [*Hanson and Mantas*, 1988]. The T_i/T_n relationships are shown in Figure 9a and they lead to the temperature profiles shown in Figure 9b that capture the essential patterns obtained by Viking. This parameterization is portrayed in pressure level units (right axis of Figure 9a) at the MGS site in order to have a general parameterization useful for different model atmospheres (e.g., at the MEX site). As an aid in the use of this scheme, we selected parameterization functions that included vastly different asymptotic limits at high and low altitudes, with sharp (but smooth) transitions between them. These parameterizations were mathematically developed in-house as:

$$R(z) = \left(2 - e^{\frac{z-z_T}{\Delta z_{T1}}}\right) * \frac{R_L - R_H}{2} + R_H \quad \text{for } z < z_T, \qquad (10)$$

$$R(z) = \left(e^{\frac{-(z-z_T)}{\Delta z_{T2}}}\right) * \frac{R_L - R_H}{2} + R_H \quad \text{for } z \geq z_T,$$

where R(z) is the ratio of either T_e or T_i to T_n, z is altitude. The parameter z_T is the central transition altitude corresponding to a pressure of 5×10^{-8} Pa for ions and 7×10^{-6} Pa for electrons. Δz_{T1} and Δz_{T2} are the asymmetric ranges (in km) over which the transition occurs. R_L and R_H are the values of the ratio at low and high altitudes, respectively. The parameterizations in Figure 9a for T_e have z_T = 171 km, Δz_{T1} = 7.5 km, Δz_{T2} = 175 km, R_L = 1 and R_H = 10. For the T_i parameterization z_T = 260 km, Δz_{T1} = 20 km, Δz_{T2} = 55 km, R_L = 1 and R_H = 9.

[41] For simplicity, we used these parameterizations for both the MGS and MEX runs, i.e., without additional dependences upon the solar zenith angle difference at the two sites.

[42] The results of the electron temperature changes produced on the simulated MGS and MEX $N_e(h)$ profile are shown in Figure 10. As anticipated, the reduction in chemical loss causes an increase in the electron densities at all altitudes near and above the M2 peak, i.e., where T_e diverges from T_n. For the MGS case, the height of the M2 peak is improved, as is the magnitude of the peak electron density. Similar improvements occur at the MEX site. With thermal equilibrium in effect at the M1-layer, no changes are seen. Thus, while use of more realistic electron temperature values cannot solve the electron density magnitude problems for *both* the M1- and M2-layers, it is clearly a needed factor for the M2-layers.

4.3.3. Effects of Secondary Ionization

[43] The final process explored deals with the fact that high energy photons that ionize an atom or molecule impart

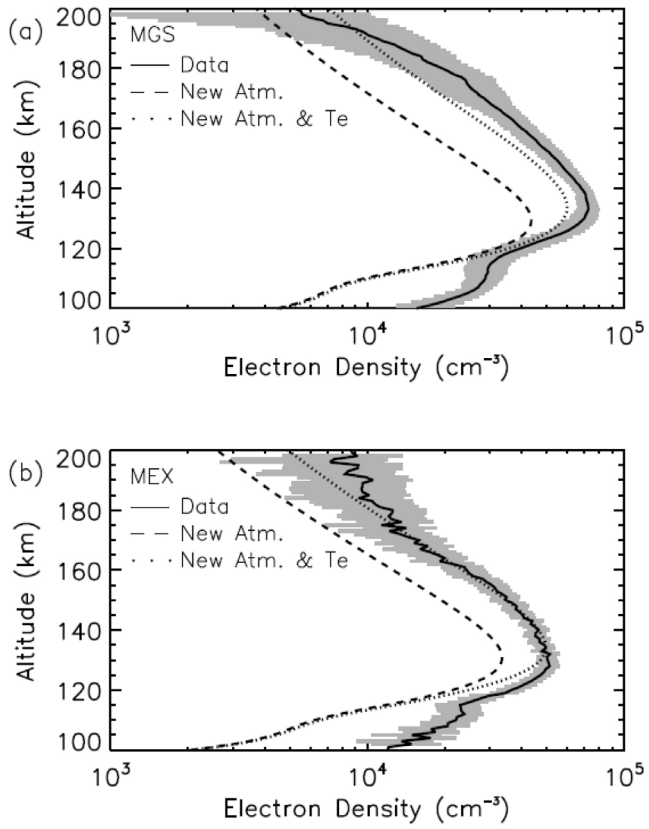

Figure 10. Results from the plasma temperature studies for (a) MGS and (b) MEX. The solid lines with shadings give observations, and the dashed lines give model results for the tuned neutral atmosphere and thermal equilibrium ($T_e = T_i = T_n$) from Figure 7. The dotted lines given model results with $T_e(z) = R_e(z) \times T_n(z)$ and $T_i(z) = R_i(z) \times T_n(z)$, where $R_e(z)$ and $R_i(z)$ are the height dependent factors shown in Figure 9a and quantitatively in equation (10).

to the liberated electron a large amount of energy. These "photo-electrons" then collide with ambient neutrals and create additional ionizations. The end result of the full cascade process is termed "secondary ionization." A complete treatment of this process using computer simulation methods has been done for the Earth and for several planets. *Galand et al.* [2009] have summarized the overall approaches used. As mentioned above when discussing thermal balance, such transport codes are complex and computer time intensive, and thus many modelers seek ways to simplify the simulation scheme by so-called "parameterization" methods [*Moore et al.*, 2009]. A convenient way to do this is to compute the primary electron density production rate versus altitude from the solar irradiance conditions of interest and then multiply that result by an altitude-dependent "ionization efficiency" function. This was the approach adopted for the original Mars model by *Martinis et al.* [2003].

[44] Figure 11 shows the secondary ionization profile used in the current model. As done previously by *Martinis et al.* [2003], it is based on the rigorous set of calculations by *Fox et al.* [1996] that led to asymptotic values at high and low altitudes, with a sharp transition near the height of the M1 peak. We added to this pattern based on *Fox et al.* [1996] a solar zenith angle dependence by using the recent study of *Nicholson et al.* [2009]. The results are expressed as a function of pressure levels so that they might be applied to different neutral atmospheres (i.e., 'ionization efficiency' being essentially an "optical depth" process). The functional form of the parameterization is given by:

$$R(P) = \left(2 - e^{\frac{-P_T}{\Delta P_T/2}}\left(1 - e^{\frac{P}{\Delta P_T/2}}\right)\right) * \frac{R_L - R_H}{2} + R_H \text{ for } \mathrm{P} < \mathrm{P_T}, \tag{11}$$

$$R(P) = \left(e^{\frac{-(P-P_T)}{\Delta P_T}}\right) * \frac{R_L - R_H}{2} + R_H \text{ for } \mathrm{P} \geq \mathrm{P_T},$$

where R(P) is the ratio of secondary to primary photoionization as a function of pressure P, P_T is the transition pressure, ΔP_T is the pressure range over which the pressure transition occurs, R_L and R_H are the values of the ratios at low and high pressures respectively. By trial and error, we arrived at an optimal set of parameters for use of these equations.

[45] For pressures lower than $\sim 6 \times 10^{-4}$ Pa, the secondary to primary ionization ratio (R_L) is 0.3, meaning that total production is 1.3 times that computed from primary solar ionization (higher than in the work by *Nicholson et al.* [2009]). At pressures higher than $\sim 10^{-2}$ Pa, the ratio R_H of 11 gives a total production function that is twelve times the computed primary ionization (lower than in work by *Nicholson et al.* [2009]). Between these two asymptotic regimes, there is a very steep, though smooth, function centered on a transition pressure P_T with a transition range ΔP_T of 4×10^{-4} Pa for the transition. Each of these four parameters (R_H, R_L, P_T and ΔP_T) can be adjusted to explore

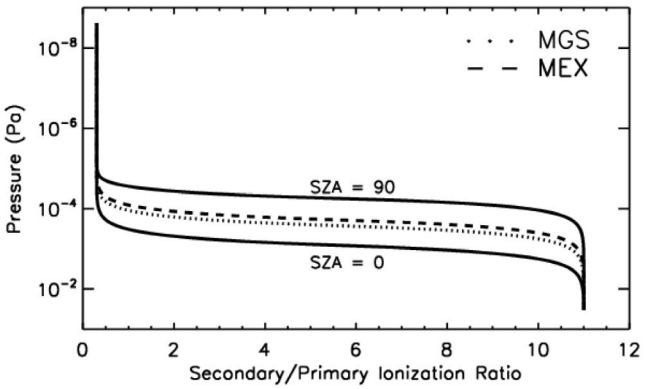

Figure 11. Parameterizations for the secondary ionization efficiency used in the model. The curves give the ratio of the number of electron-ion pairs produced by photo-electrons to the number produced from primary ionization. The solid lines show the range of efficiencies for solar zenith angles from 0° to 90° solar zenith angles. The dotted line gives the case for MGS observations, and the dashed line for MEX conditions. The vertical scale is in pressure units to allow adaptation to any neutral atmosphere (see text). For example, the relationship between pressure levels and heights at the MGS location are the same as in Figure 9.

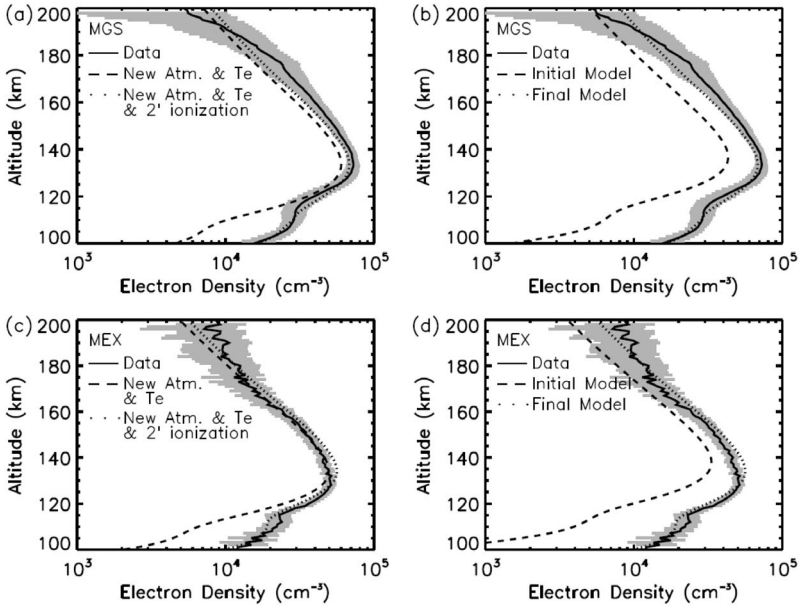

Figure 12. The results of the secondary ionization experiments for (a) MGS and (c) MEX. The solid line profiles are the observations. The dashed curves give the results from the neutral atmosphere and non-thermal equilibrium profile from Figure 9. The dotted-line curves give the final simulation results that incorporate the secondary-ionization parameterization scheme from Figure 11 and equations (11) and (12). (b and d) The initial and final simulations for MGS and MEX respectively.

other possibilities. Upon doing several tests, we found that the transition pressure was the key parameter to examine, with the transition width being next in importance.

[46] The final adjustment needed is to realize that the transition pressure (P_T) of our secondary ionization parameterization will change with solar zenith angle (χ), as described in detail by *Nicholson et al.* [2009]. Adapting their formulation (equation 13) to our parameterization scheme is straightforward, resulting in the following:

$$P_T(\chi) = P_{\min} + \alpha\cos(\chi) + \beta[\cos(\chi)]^{1/2} \qquad (12)$$

where, $P_{min} = 5.57 \times 10^{-5}$ Pa, $\alpha = 5.3 \times 10^{-4}$ Pa, $\beta = 2.1 \times 10^{-4}$ Pa. For χ-values larger than 90°, P_T is kept constant at the value of P_{min}.

[47] The MGS and MEX electron density profiles produced using the parameterization scheme above are shown in Figure 12. One can see that this experiment provided the types of dramatic enhancements needed to obtain model values of peak densities of the M1-layer closer to those observed at the MGS and MEX points, while resulting in only a minor increase upon the M2-layers. This emphasizes once again the important role played by the soft X-ray fluxes that create the M1-layer [*Fox and Yeager*, 2006; *Haider et al.*, 2006]. These relatively simple set of functions can be applied in simulations using a selected neutral atmosphere and the full range of local times and latitudes on the sunlit hemisphere.

4.4. Summary of Model Adjustments

[48] We identified three possible ways to adjust prior 1-D simulation methods that did not reproduce adequately the observed dual-hemisphere MGS and MEX results. Our final simulation used a modified MCDB neutral atmosphere to correct optical depth layer heights at the MGS and MEX observing sites (Figure 7), together with the electron temperature adjustments to chemistry needed for improved peak density and altitude values of the M2-layer (Figure 9), and a secondary ionization adjustment needed for improved peak density values of M1 layer (Figure 11). The latter two parameterizations were assigned functional forms in pressure units (equations (10)–(12)) to enable uses under a variety of conditions. The initial and final results from the "tuned model" are shown in Figure 12 (right). These best-match simulations are acceptable for both layers, though not ideal. For M2, the peak density is slightly low for MGS and slightly high for MEX (both within observational uncertainties). The altitudes of peak density for the M2-layer are fine at both sites, though slightly high for the MEX data. For the enigmatic M1-layer, the nuances of a separate layer versus a shoulder versus an inflection point in the $N_e(h)$ profiles are difficult to quantify. The simulations are nonetheless within observational uncertainties. For the topside results, not used as a modeling constraint, simulations and data are in reasonable agreement, with the MEX simulations better matched over the full altitude range versus those for MGS.

5. Day-to-Day Variability and Diurnal Patterns

5.1. Modeled Versus Observed Variability

[49] As demonstrated in this and all previous studies of the Martian ionosphere, the altitudes of the two dominant layers are well within the photo-chemical regime. This implies that changes in solar irradiances and/or solar zenith angles should be the dominant causes of variability. This is

the case for the terrestrial E-layer [*Moore et al.*, 2006b]. For Mars, studies of MGS data sets clearly indicated photochemical dominance on a day-to-day basis, as described in the review by *Withers* [2009]. Yet, the range of local time and latitude conditions (that together determine solar zenith angles), is rather limited for MGS data. Conversely, the MEX $N_e(h)$ profiles offer sparse coverage in time and space but, when available, they vary significantly in solar zenith angle. This is precisely the case with the MEX-MGS overlap period treated in this study, as summarized in Figure 3. Clearly there was more variability in the six profiles shown in Figure 3b than in Figure 3a, and thus the subset of four central days was selected for detailed modeling. Now that we have arrived at a "tuned" average model, we apply it on a day-to-day basis to all profiles in the common observing period.

[50] As shown in Figure 3, the MGS data set corresponded to latitudes ranging from ~66° to ~74° and local times from ~4:45 to ~5:45 under northern hemisphere summer conditions, while the MEX observations ranged from latitudes of ~23° to 80° and local times from ~7:30 to ~8:40 under southern hemisphere winter conditions. Thus we now apply the parameters used to obtain the results in Figure 12 to the full range of MGS and MEX data spanning 8 December 2004 to 4 January 2005. For these runs, the solar irradiances changes each day, as shown in Figure 6a, i.e., as given by SOLAR 2000 evaluated at Mars' distance from the Sun. The results are displayed in Figure 13 using the same format and color coding as in Figure 3. The simulation patterns in Figure 13 for both observing sites offer an acceptable first approximation for the observations shown in Figure 3. For MGS, the periods before and after the data gap show the transition from low to higher M2-layer peak densities from the model. In the MEX profiles, the "outliers" before and after the central four days are also well portrayed by the model.

[51] In terms of a more quantitative assessment, the larger MGS data set is best suited to forming overall mean values for each layer, and their standard deviations. These are 2.8×10^4 $e^-cm^{-3} \pm 19\%$, and 7.9×10^4 $e^-cm^{-3} \pm 10\%$ for the peak densities of the M1 and M2-layers, respectively. The model results are 3.1×10^4 $e^-cm^{-3} \pm 10\%$, and 7.2×10^4 $e^-cm^{-3} \pm 4\%$, respectively. Thus, while the agreement in absolute densities is acceptable, the variability from the model accounts for only half of the observed variability. For a simple photochemical molecular ion layer, the resultant electron density depends on the square root of the production function [*Rishbeth and Garriott*, 1969]. Mars' ionosphere is far more complex than that, and the functional dependence between proxies for production (e.g., F10.7) and observed peak densities can be significantly different. *Fox and Yeager* [2009], for example, found the exponents to range between ~0.25–0.5 for the main and secondary layers, respectively. Whatever the exponent might be, the resultant electron density variability would be related by that exponent to the photon flux variability. For our model, the variability of production is dominated by the variability in solar irradiance which, from Figure 6, corresponds to 15–28% for wavelength bins #1 and #2 (λ = 1.86–4.92 nm) responsible for the M1-layer, and 1–10% for the EUV wavelength bins #7–11 (λ = 25.63–30.38 nm) mostly responsible for the peak density of the M2-layer. For the square root (0.5) case, this comes to ~7–14% for the M1-layer and ~5% for the M2-layer. Thus the source of variability in the model is clearly identified – it is due to the variability of solar irradiance.

[52] Such results are encouraging for the use of simple 1-D models, with parameterizations schemes for critical processes, to study day-to-day variability sources and effects. Yet, additional complexities are required to pursue the full scope of observed day-to-day variability effects. These include neutral atmospheres and winds versus local time, latitude, longitude and season, coupled to the variety of electro-dynamical processes associated with crustal magnetic field locations and solar wind conditions. For Earth, this has been started with GCMs run for a full year, with input parameters changing on scales ranging from every three hours to daily [*Rishbeth et al.*, 2009; *Mendillo et al.*, 2010]. GCMs for Mars are well-suited to begin such studies.

5.2. Diurnal Context

[53] The results given for the MGS and MEX observations and their simulations in Figures 12 and 13 pertain to the dawn period, perhaps the most difficult time of day for an ionospheric model to be tested [*Fox and Yeager*, 2006]. To place these results into the context of the diurnal behavior of the ionosphere at Mars, we show in Figure 14 the diurnal curves for the maximum electron densities of the M1 and M2-layers that come from model runs for a full Martian day. These incorporate all of the adjustments made to achieve the results in Figure 12, including the full range of solar zenith angle dependences for the parameterization of secondary ionization via equation (7).

[54] There are no data sets available for diurnal patterns of the M1 and M2 peak electron densities at Mars. The model curves in Figure 14 thus show how the Martian ionosphere would appear if measured continuously under northern hemisphere summer and southern hemisphere winter conditions, at the latitudes of MGS and MEX, respectively. Solar zenith angles clearly have dramatic effects upon photo-chemical layers. In Figure 14a, a high latitude (67°N) summer ionosphere shows the effects of many hours of sunshine, in marked contrast to the conditions in Figure 14b of a midlatitude (45°S) winter ionosphere. The only possible times of MGS/MEX data-model comparison (post-sunrise) are shown and they are, by design, in good agreement since the model was tuned to do so. Perhaps surprising are the noontime values that do not show vastly different electron densities between the M1 and M2-layers. It is interesting to note that if noon and midnight data were available, the constraints offered to models would be far more severe. Yet, given the absolute magnitude limitations of the radio occultation methods, reliable data might only be possible for daytime hours (and at night only for the summer solstice conditions). The nighttime magnitudes of the peak densities of the M2-layer under winter solstice conditions are below typical instrument measurement possibilities (~10^3 e^- cm^{-3}). For topside radio sounding methods (e.g., MARSIS on MEX), however, observations are possible for all magnitudes of the M2-layer, but the M1-layer would remain inaccessible. The upcoming MAVEN mission to explore atmospheric escape processes on Mars may produce data

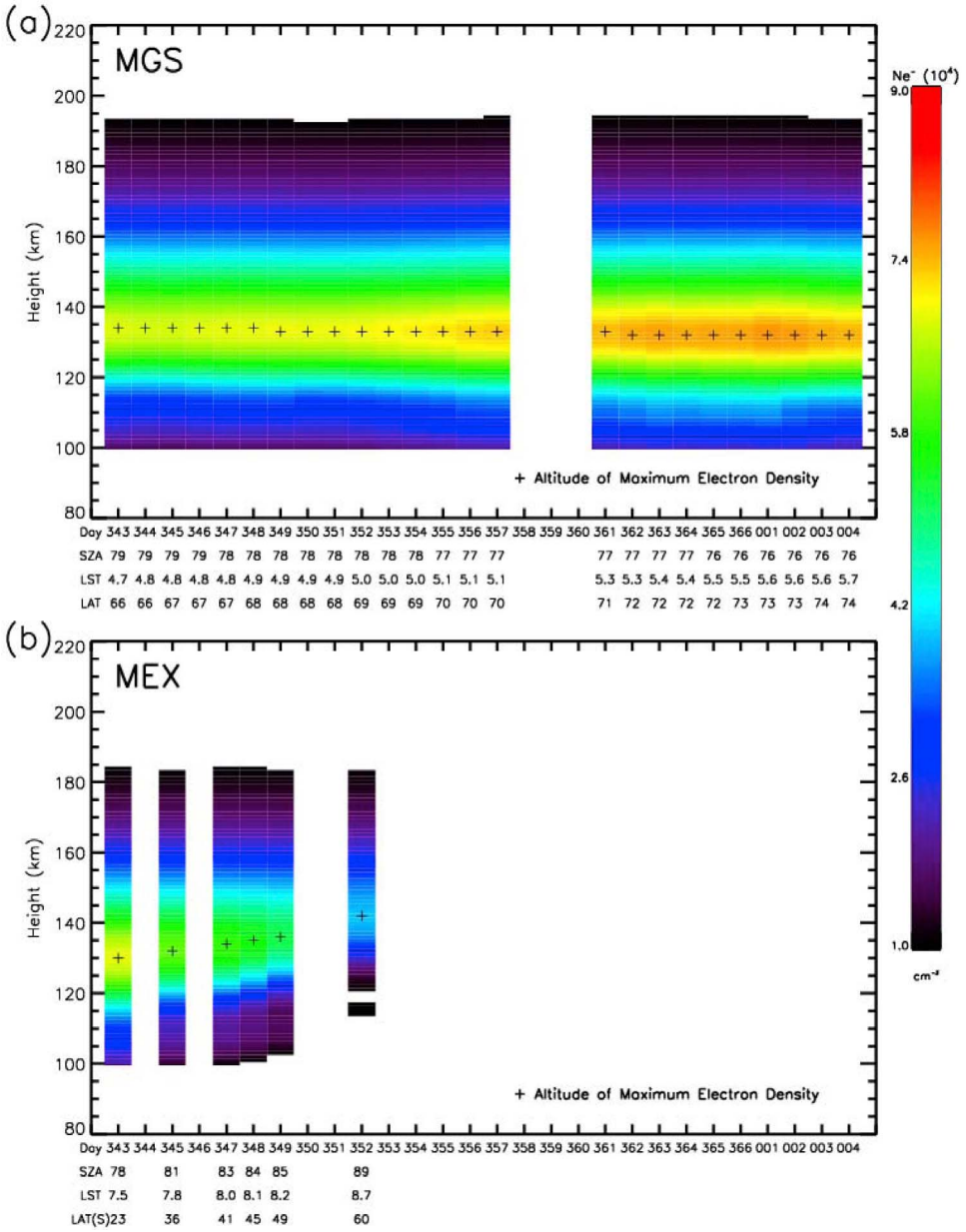

Figure 13. Simulation results for the full set of observations shown in Figure 3 using the set of parameters derived in this study. Note that the simulations used the same neutral atmospheres from Figure 7 at each site, and solar zenith angles and irradiances that changed daily (see text).

sets for peak density under a broad set of LT conditions, but unfortunately will not have access to the M1-layer.

6. Discussion

6.1. Photo-Chemistry Versus Plasma Diffusion

[55] With all of the adjustments made to maximize agreement between model and data, we now use these optimal parameters to explore the basic roles of chemistry versus dynamics. To do this, we take the "successful" simulations for the M1 and M2 layers shown in Figure 12 that included photo-chemistry-only, i.e., use of equation (1), and re-run them over the altitude regime 80–350 km with dynamics included (equation (2)). Thus, at each height, production and loss no longer operate in isolation of what occurs above and below. While diffusion model runs were conducted for both MGS and MEX cases, only the latter is described here. The results are presented in Figure 15 for the MEX case, chosen because MEX radio occultation observations extend to heights above 200 km. Figure 15a shows the resultant electron density profiles for the photo-chemical equilibrium solution (dotted line) and the chemistry-plus-plasma diffusion solution (dashed line). The dark gray line gives the average of the four days (five profiles) of MEX data, with the light gray shading to show observational uncertainties. Figure 15b shows the ion composition results

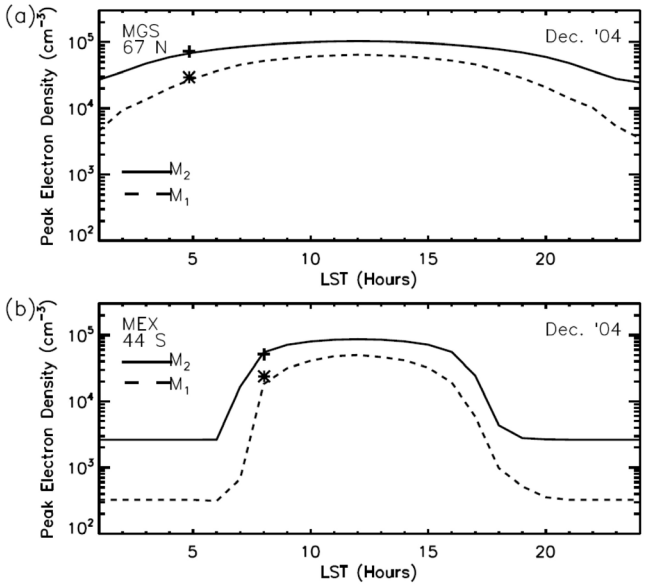

Figure 14. The full diurnal curves for the peak densities of the M1 and M2-layers from the simulations tuned to match near-dawn observations by (a) MGS and (b) MEX. In each panel, the upper curve gives peak density of the M2-layer versus LT and the dashed curve gives peak density of the M1-layer versus LT. The plus-signs and asterisks give their respective observations from MGS and MEX. In Figure 14b, electron densities stabilize at near-midnight local times as the SZA exceeds 90°.

from the photo-chemistry only run. Figure 15c shows the ion composition results from the photo-chemistry-plus-diffusion run. Clearly, the build-up of O^+ concentrations in the topside does not occur when plasma diffusion is included. For heights below ~170 km, there is no separation between the two model profiles in Figure 15a, showing once again that the two main layers of the Martian ionosphere are dominated by photo-chemistry, at least under the average type conditions used here. The agreement at topside heights between observations and model results that include plasma diffusion is somewhat surprising given that only vertical diffusion is included in the model. This suggests that effects upon plasma transport caused by the presence of crustal and/or draped magnetic fields appear to be minimal, at least for this set of dawn observations during a period of quiet solar wind conditions. We explore the possible reasons for this next.

6.2. Roles of Magnetic Fields

[56] Much has been written about the behavior of an ionosphere on a planet without a global magnetic field, i.e., Venus and Mars. Broad introductions appear in work by *Schunk and Nagy* [2009], with references to the fundamental papers on the topic. A recent comparison of MHD models for Mars appears in work by *Brain et al.* [2010]. Following the discovery of crustal fields at Mars, emphasis switched from how solar wind "draped" magnetic fields affected the ionosphere to how intrinsic fields did so. The works of *Crider et al.* [2001] and *Krymskii et al.* [2002] give concise introductions to the topic, done within the contexts of earlier

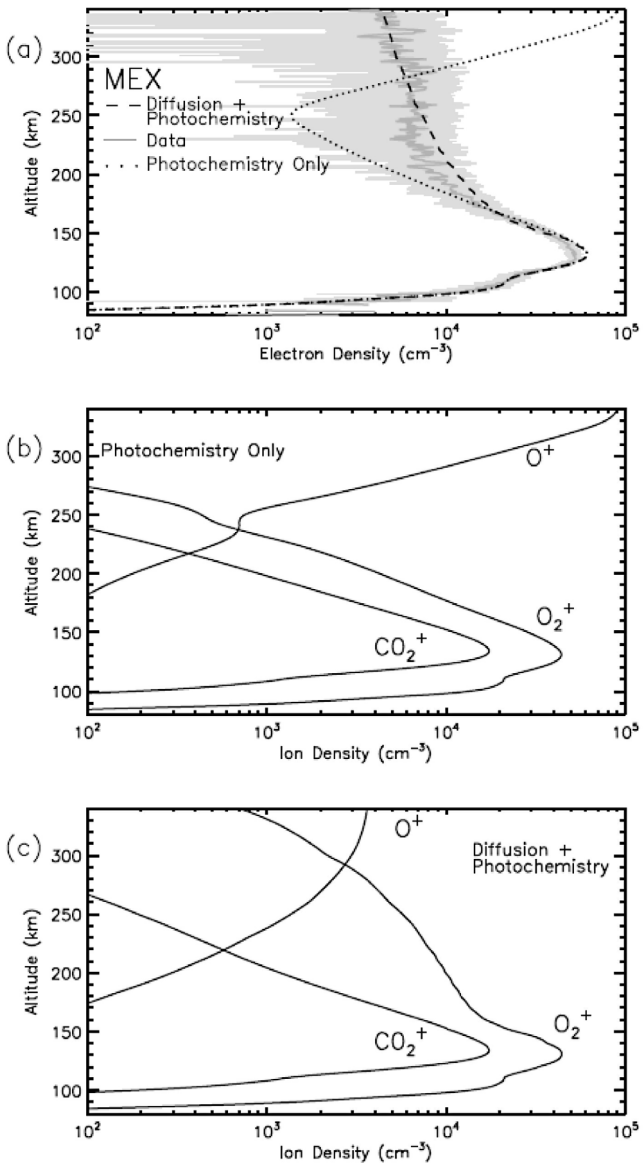

Figure 15. Results from simulation experiments that compare N_e (h) profiles derived using photo-chemical-only versus photo-chemistry plus plasma diffusion for MEX location. Using the updated model parameters that led to the final N_e(h) profiles (dotted-lines) in Figure 12d, a model run with photo-chemistry and plasma transport was conducted for the MEX data set. (a) The resultant electron density profiles with (dashed line) and without (dotted line) plasma diffusion. The dark gray line gives the MEX N_e(h) average profile with observational uncertainly levels given by the light gray shading. Photo-chemistry dominates for the M1 and M2-layers below ~170 km. (b) The ion composition profiles that collectively add to form the photochemistry-only electron density profile. (c) The corresponding ion composition results from the photo-chemistry-plus-diffusion run. The profiles of the dominant ions add to yield the N_e(h) profile shown by the dashed line in Figure 15a. The topside photo-chemical layer of O^+ ions that develops in the photo-chemistry-only run does not exist due to a combination of chemical and plasma diffusion processes (see text).

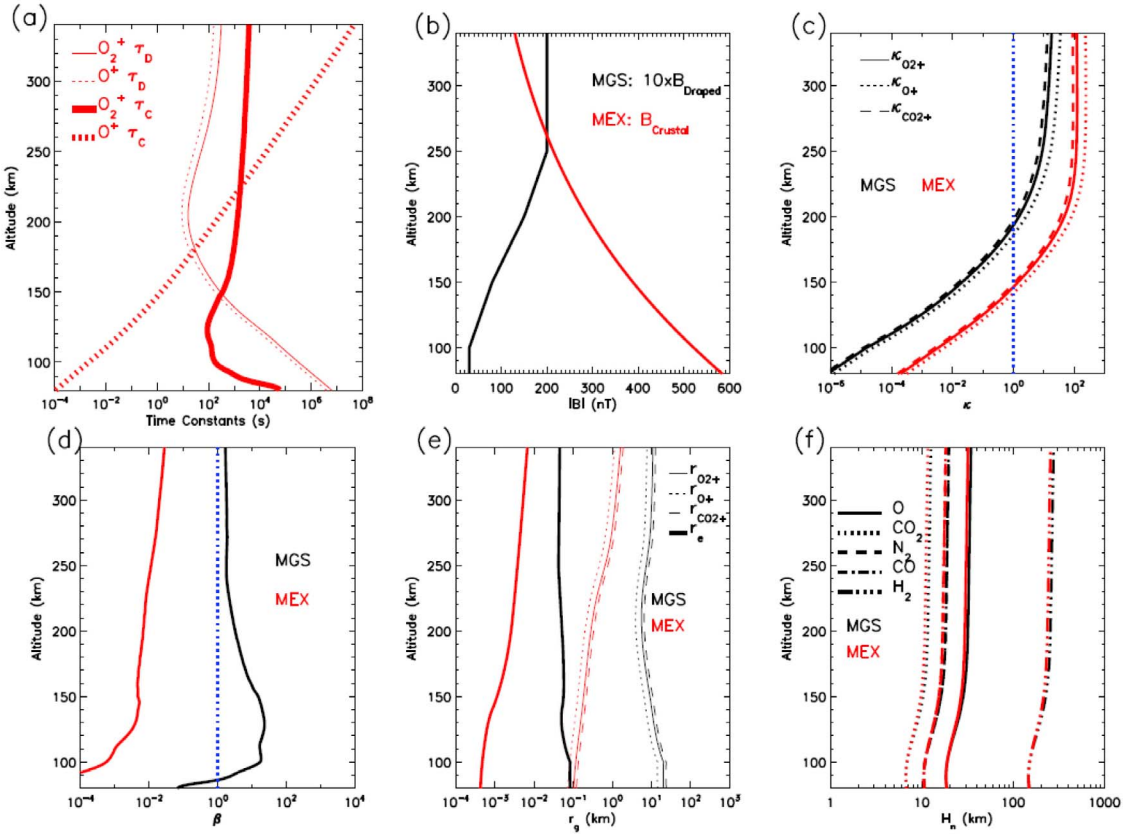

Figure 16. A summary of time constants, magnetic fields, characteristic frequencies, and scale length parameters for plasmas and neutrals used to assess various aspects of photo-chemistry and plasma dynamics. Black and red curves are used to distinguish between the MGS (northern hemisphere) and MEX (southern hemisphere) locations. (a) The diffusion (thin line) and photochemical (thick line) time constants, τ_D and τ_C, of O_2^+ (solid) and O^+ (dashed), respectively. The values for MGS were very similar to those for MEX and so only the latter are shown for visibility. (b) The magnetic field magnitudes taken to represent the conditions in the northern (black) and southern (red) hemispheres. A weak, draped field is adopted for the northern hemisphere (multiplied by 10 for visibility) and a crustal field is adopted for the southern hemisphere, consistent with Figure 2. (c) κ, the ratio of gyro to collision frequency of O_2^+, O^+, and CO_2^+. The blue vertical line denotes a κ of unity, indicating the region where the gyro frequency and collision frequency are comparable. (d) β, the ratio of plasma thermal pressure to magnetic pressure for our modeled electron densities, plasma temperatures, and magnetic fields. The blue vertical line denotes a β of unity. Calculated values are shown in black for MGS and in red for MEX. (e) The gyroradii for electrons and for the two dominant ions at the MGS and MEX sites and (f) the scale heights of the neutral atmosphere species at both locations (see text).

studies by *Shinagawa and Cravens* [1989, 1992]. The consensus message to emerge from all of those studies was that the role of **B**-fields became increasingly important the higher in altitude above the photo-chemical layers. While the Martian topside ionosphere is not the topic of the present study, it is important to outline the complexities that emerge within just a few scale heights of the M2-layer. In doing so, we note that the dawn period used in this study might represent a solar wind – planet geometry that minimizes effects of a draped **B**-field upon the ionosphere [*Crider et al.*, 2001].

[57] We begin our examination of the domains of chemistry and dynamics in Figure 16 using several species-dependant characteristic time constants and scale length parameters within the model. These are $\tau_D = \frac{H_n^2}{D_a}$ is the diffusion time constant, $\tau_C = \frac{1}{R}$ is the photochemical time constant, $\kappa = \frac{qB/m_s}{\sum_n \nu_{sn}}$ is the ratio of gyro to collision frequency, $\beta = \frac{n_e k T_p}{B^2/2\mu_o}$ is the ratio of plasma thermal pressure to magnetic pressure, $r_g = \frac{\sqrt{kT_s/m_s}}{qB/m_s}$ is the gyroradius and $H_n = \frac{kT_n}{m_n g}$ is the neutral scale height. D_a is the ambipolar diffusion coefficient given earlier. R is the chemical loss rate of each ion species from equation (1), q is the charge, B is the magnetic field strength, m is the mass, and ν is the collision frequency. Ion-neutral collision frequencies are taken from *Banks and Kockarts* [1973], and electron-neutral collision frequencies are taken from *Schunk and Nagy* [2000]. n_e is the electron density, k is Boltzmann's constant, T is the temperature, μ_o is the permeability of free space and g is the gravitational acceleration. Subscript s refers to ions or

electrons, subscript n refers to neutrals and subscript p refers to plasma.

[58] We start in Figure 16a with the time constants for diffusion (τ_D) and chemistry (τ_C) for the MEX conditions since they provide the best source for data comparisons over a broad range of altitudes. In Figure 16a, the τ_D values for O_2^+ (shown by the thin solid line) become smaller than τ_C values (the thick solid line) at altitudes above 150 km. For O^+ (thin and thick dotted lines), the same can be said for altitudes greater than 170 km. Above these heights, diffusion processes for O_2^+ and O^+, respectively, become faster than photochemical processes and thus plasma transport must be considered. Given that O^+ is the dominant ion in the topside ionosphere, the divergence between photochemistry-only and chemistry-plus-diffusion shown in Figure 15a follows from these time constant results.

[59] Moving beyond the results from Figure 16a, i.e., that collisions with atmospheric species dominate below 170 km and plasma diffusion above, we next consider the degree to which magnetic fields influence plasma flow. The key question is to what extent plasma diffusion proceeds vertically through a neutral atmosphere versus being constrained to move along magnetic field lines, even when **B** is very weak. We frame such a discussion within the context of the characteristic times and scale lengths given above. Results in Figures 16b–16f shown in red refer to the use of the MEX atmosphere and ionosphere, while those shown in black pertain to the MGS conditions.

[60] Figure 16b shows typical magnetic field conditions for the altitude range relevant to our model. In the northern hemisphere, crustal fields are scarce and the solar wind interaction with the planet creates a draped effect for the interplanetary magnetic field. In the southern hemisphere, crustal fields exist and we show a representation of a **B**(h) case, where h is altitude, that is consistent with a strong crustal field source [*Brain et al.*, 2003; *Arkani-Hamed*, 2004]. The magnetic fields in Figure 16b were used to compute gyro frequencies, gyro radii and magnetic field pressures. In Figure 16c, κ, the ratios of gyro frequency to collision frequency, are shown for O_2^+ (solid line), O^+ (dotted line) and CO_2^+ (dashed line) for the MGS (black) and MEX cases (red). Also shown is a vertical blue dotted line at $\kappa = 1$. The $\kappa \sim 1$ altitude represents the upper boundary of the dynamo region below which ions and electrons are influenced differently by magnetic fields, and above which plasma becomes increasingly influenced by magnetic fields [*Withers*, 2008]. For the modeled MGS electron density profiles in the northern hemisphere, $\kappa = 1$ at ~190 km indicating a greater influence of draped fields on the ionosphere above that altitude, and less below it. For MEX electron density modeled profiles, $\kappa = 1$ at ~150 km, indicating that magnetic fields become more important for plasma processes above that altitude. We conclude from these results that the peak electron densities of the M1 and M2-layers computed in the model are robust simulations for these altitudes, i.e., the presence of magnetic fields are of minor importance at the heights of both layers.

[61] In Figure 16d we show the plasma β parameter (ratio of plasma thermal pressure to magnetic pressure) as another way to assess the importance of the magnitude of the magnetic field on plasma processes. A $\beta < 1$ indicates either a region of rarified plasma and/or a region dominated by magnetic fields. Conversely, $\beta > 1$ indicates a region dominated by thermal plasma processes and/or one of negligible magnetic field. A vertical blue dotted line is shown at $\beta = 1$ for reference. At the height of our modeled maximum electron density, and using a strong Martian magnetic field of ~400 nT from Figure 16b for MEX, β is between 10^{-3} and 10^{-2} (in contrast to ~10^{-4} to 10^{-5} at the peak of the Earth's ionosphere). The plasma in the M2-layer is not rarified and such β values imply that for the strongest magnetic fields at Mars, field aligned diffusion should start to become important for transport. Yet, as shown in Figures 16a and 15, diffusion itself does not affect N_e(h) below ~170 km. Above that height, as shown in Figure 15a, there is a reasonable agreement with MEX data when only vertical diffusion is included in the model for heights below ~350 km. For the MGS site, using a weak Martian field of ~10 nT for B in the northern hemisphere, β is >1. This implies that **B** is too weak to impose a direction upon plasma diffusion at the ionospheric heights being modeled.

[62] Finally, in Figures 16e and 16f we show two characteristic lengths (gyroradii and neutral scale heights) for the MGS and MEX conditions. For heights below ~150 km, the gyroradius for the dominant ion (O_2^+) is ~10 km for the MGS location, only slightly above the scale height (7–9 km) of the dominant neutral (CO_2). For the MEX location, the gyroradii below ~150 km are at least an order of magnitude smaller than the neutral scale height of CO_2. These are additional indicators that plasma diffusion controlled by magnetic fields should be important, but they relate to altitudes where diffusion itself is not important. For the topside altitudes (h > ~200–350 km), where the neutral scale height is due to molecular hydrogen (see Figure 7), the gyroradii are all smaller than the neutral scale height, and thus field-aligned diffusion should be dominant. The fact that vertical diffusion in the model matches the only observational data for topside patterns remains unresolved. Three possible considerations that deal with chemistry, dynamics and observational techniques are now treated.

[63] The realization that molecular hydrogen is an important constituent in the Martian topside ionosphere has been a somewhat recent finding [*Fox*, 2003]. The reaction between O^+ and H_2 (leading to OH^+ and H) is one that proceeds at nearly the gas kinetic rate (1.35×10^{-9} cm^3 s^{-1}) and thus it is as efficient as reaction (7) in Table 1a that converts O^+ to O_2^+. The transformation of atomic ions to molecular ions is important because molecular ions recombine with electrons far more rapidly than atomic ions do. For the terrestrial ionosphere where O^+ is the dominant ion, the abundances of H_2, H_2O and CO_2 are not important species in the thermosphere. They are, however, the major constituents of the exhaust plumes of large rockets—which led to the discovery of their so-called "ionospheric hole-making" capabilities [*Mendillo et al.*, 1975, 1987, 2008]. Subsequently, the role of H_2O as a natural catalyst within the ionosphere at Saturn was explored [*Moore et al.*, 2006a; *Moore and Mendillo*, 2007]. *Fox* [2003] did the same for H_2 within the Martian ionosphere, pointing out the crucial role it plays in the chemistry near the peak and in the topside ionosphere. The H_2 altitude profiles used in our model (shown in Figure 7) point to another facet of its role, namely, as the dominant neutral species through which

plasma diffusion occurs. Models that do not take such H_2 profiles (i.e., a column of essentially constant density) into consideration [e.g., *Nicholson et al.*, 2009; *Najib et al.*, 2011] result in diffusion coefficients that grow exponentially with height, i.e., following the atomic oxygen pattern. These result in un-realistically high estimates for diffusion speeds (>10 km/sec), and thus to un-realistic topside profiles. Additional work is clearly needed to account for both the chemical and dynamical effects that molecular hydrogen causes in the topside ionosphere of Mars. For the results presented here, such processes do not affect the M1 and M2 layers.

[64] A final consideration about the apparent agreement between the MEX observations and the model results shown in Figure 15a deals with observational conditions. During radio occultation experiments, the raypath geometry results in averaging over horizontal spatial scales that far exceed the altitude span of the derived $N_e(h)$ profiles. Perhaps observations that integrate over magnetic inclination angles of crustal **B**-fields that vary significantly over small spatial scales result in derived profiles that mimic an ionosphere unaffected by magnetic fields.

7. Summary

[65] One dimensional models have a rich history of contributions to our understanding of the photo-chemical processes that govern the two main layers of the Martian ionosphere. Subsequent three dimensional general circulation models (GCMs) and MHD codes have built upon these to portray the full scope of the solar and solar wind control of Mars' upper atmosphere and ionosphere. In this paper, we returned to the 1-D approach with the goal of improving simulation methods by the challenges of new data sets that provide electron density profiles simultaneously at locations in both hemispheres. These same-day observations were examined in detail and used to select modeling targets. Central to the study was the fact that same-day data require the use of a single solar irradiance pattern, eliminating any "tuning" of solar input as a free parameter.

[66] Selection of the neutral atmospheres to use at each simulation site, and how to handle the key processes of secondary ionization and electron temperature control of chemical loss, were then formulated in ways to permit parameterizations of both processes. The resultant system offers for the first time a unified, flexible, and systematic way to conduct simulations at any location, local time, season, dust level and solar cycle condition.

[67] The results obtained showed that the main peak magnitude of the Martian ionosphere is due to three components: direct photo-ionization, enhanced by ~30% due to secondary ionization, and increased further by an increase in electron temperatures which reduces the chemical loss rates. The secondary layer is due to two processes: direct photo-ionization, with production enhanced by an order of magnitude by ionization by the photoelectrons created in the primary ionization process. Plasma dynamics is of negligible importance for simulations of the peak electron densities of both the M1 and M2-layers. Using this approach, simulations of day-to-day variability were conducted and achieved success given the limitations of the model.

[68] Somewhat un-anticipated was the finding that the roles of solar wind-draped and planetary crustal magnetic fields do not need to be considered in simulations of the average peak electron densities under the quiescent conditions examined here. Future work is needed for the topside ionosphere, where the roles of H_2 plasma-neutral chemistry, plasma dynamics, plasma instabilities, energetic particle precipitation and magnetic field topologies have greatly increased importance.

[69] **Acknowledgments.** We thank Professor Jane Fox and anonymous referees for their constructive advice and suggestions. This work was supported, in part, by NASA grants to Boston University from the Mars Data Analysis Program (MDAP NNX07AN99G), Mars Fundamental Research Program (MFRP NNX08AN56G) and from the Living with a Star Program (LWS NNX08AP96G).

[70] Masaki Fujimoto thanks the reviewers for their assistance in evaluating this paper.

References

Arkani-Hamed, J. (2004), A coherent model of the crustal magnetic field of Mars, *J. Geophys. Res.*, *109*, E09005, doi:10.1029/2004JE002265.

Banks, P., and G. Kockarts (1973), *Aeronomy*, Academic, San Diego, Calif.

Bougher, S. W., S. Engel, D. P. Hinson, and J. M. Forbes (2001), Mars Global Surveyor Radio Science electron density profiles: Neutral atmosphere implications, *Geophys. Res. Lett.*, *28*, 3091–3094, doi:10.1029/2001GL012884.

Bougher, S. W., S. Engel, D. P. Hinson, and J. R. Murphy (2004), MGS Radio Science electron density profiles: Interannual variability and implications for the Martian neutral atmosphere, *J. Geophys. Res.*, *109*, E03010, doi:10.1029/2003JE002154.

Bougher, S., et al. (2009), Neutral upper atmosphere and ionosphere modeling, in *Comparative Aeronomy*, *Space Sci. Ser.*, vol. 29, edited by A. Nagy et al., pp. 107–141, Springer, New York.

Brain, D. A., F. Bagenal, M. H. Acuña, and J. E. P. Connerney (2003), Martian magnetic morphology: Contributions from the solar wind and crust, *J. Geophys. Res.*, *108*(A12), 1424, doi:10.1029/2002JA009482.

Brain, D., et al. (2010), A comparison of global models for the solar wind interaction with Mars, *Icarus*, *206*, 139–151, doi:10.1016/j.icarus.2009.06.030.

Chamberlain, J. W. (1962), Upper atmospheres of the planets, *Astrophys. J.*, *136*, 582–593, doi:10.1086/147409.

Chamberlain, J. W., and D. M. Hunten (1987), *Theory of Planetary Atmospheres*, Academic, Orlando, Fla.

Chen, R., T. Cravens, and A. Nagy (1978), The Martian ionosphere in light of the Viking observations, *J. Geophys. Res.*, *83*, 3871–3876, doi:10.1029/JA083iA08p03871.

Choi, Y., J. Kim, K. Min, A. Nagy, and K. Oyama (1998), Effects of the magnetic field on the energetics of Mars, *Geophys. Res. Lett.*, *25*, 2753–2756, doi:10.1029/98GL51839.

Colegrove, F. D., F. S. Johnson, and W. B. Hanson (1966), Atmospheric composition in the lower thermosphere, *J. Geophys. Res.*, *71*, 2227–2236.

Crider, D., et al. (2001), Magnetic field draping around Mars: Mars Global Surveyor results, *Adv. Space Res.*, *27*, 1831–1836, doi:10.1016/S0273-1177(01)00333-7.

Forget, F., F. Hourdin, R. Fournier, C. Hourdin, O. Talagrand, M. Collins, S. R. Lewis, P. L. Read, and J.-P. Huot (1999), Improved general circulation models of the Martian atmosphere from the surface to above 80 km, *J. Geophys. Res.*, *104*, 24,155–24,175, doi:10.1029/1999JE001025.

Fox, J. L. (1993), The production and escape of nitrogen atoms on Mars, *J. Geophys. Res.*, *98*, 3297–3310, doi:10.1029/92JE02289.

Fox, J. L. (2003), Effect of H2 on the Martian ionosphere: Implications for atmospheric evolution, *J. Geophys. Res.*, *108*(A6), 1223, doi:10.1029/2001JA000203.

Fox, J. L., and A. Dalgarno (1979), Ionization, luminosity and heating of the upper atmosphere of Mars, *J. Geophys. Res.*, *84*, 7315–7333, doi:10.1029/JA084iA12p07315.

Fox, J., and K. Yeager (2006), Morphology of the near-terminator Martian ionosphere: A comparison of models and data, *J. Geophys. Res.*, *111*, A10309, doi:10.1029/2006JA011697.

Fox, J., and K. Yeager (2009), MGS electron density profiles: Analysis of the peak magnitudes, *Icarus*, *200*, 468–479, doi:10.1016/j.icarus.2008.12.002.

Fox, J., P. Zhou, and S. Bougher (1996), The Martian thermosphere/ionosphere at high and low solar activities, *Adv. Space Res.*, *17*, 203–218, doi:10.1016/0273-1177(95)00751-Y.

Fox, J., M. Galand, and R. Johnson (2008), Energy deposition in planetary atmospheres by charged particles and solar photons, *Space Sci. Rev.*, *139*, 3–62, doi:10.1007/s11214-008-9403-7.

Galand, M., L. Moore, B. Charnay, I. Müller-Wodarg, and M. Mendillo (2009), Solar primary and secondary ionization at Saturn, *J. Geophys. Res.*, *114*, A06313, doi:10.1029/2008JA013981.

Gurnett, D. A., et al. (2005), Radar sounding of the ionosphere of Mars, *Science*, *310*, 1929–1933, doi:10.1126/science.1121868.

Gurnett, D. A., et al. (2010), Large density fluctuations in the Martian ionosphere as observed by the Mars Express radar sounder, *Icarus*, *206*, 83–94, doi:10.1016/j.icarus.2009.02.019.

Haider, S., S. Seth, V. Choksi, and K. Oyama (2006), Model of photoelectron impact ionization with the high latitude ionosphere at Mars: Comparison of calculated and measured electron density, *Icarus*, *185*, 102–112, doi:10.1016/j.icarus.2006.07.010.

Haider, S. A., M. A. Abdu, I. S. Batista, J. H. Sobral, E. Kallio, W. C. McGuire, and M. I. Verigin (2009), On the response of solar X-ray flare and coronal mass ejection in the ionosphere of Mars and Earth, *Geophys. Res. Lett.*, *36*, L13104, doi:10.1029/2009GL038694.

Haider, S. A., S. P. Seth, D. A. Brain, D. L. Mitchell, T. Majeed, and S. W. Bougher (2010), Modeling photoelectron transport in the Martian ionosphere at Olympus Mons and Syrtis Major: MGS observations, *J. Geophys. Res.*, *115*, A08310, doi:10.1029/2009JA014968.

Hanson, W., and G. Mantas (1988), Viking electron temperature measurements: Evidence for a magnetic field in the Martian atmosphere, *J. Geophys. Res.*, *93*, 7538–7544, doi:10.1029/JA093iA07p07538.

Hanson, W., S. Sanatani, and D. Zuccaro (1977), The Martian ionosphere as observed by the Viking retarding potential analyzers, *J. Geophys. Res.*, *82*, 4351–4363, doi:10.1029/JS082i028p04351.

Hinson, D., R. Simpson, J. Twicken, G. Tyler, and F. Flasar (1999), Initial results from radio occultation measurements with Mars Global Surveyor, *J. Geophys. Res.*, *104*, 26,997–27,012.

Hinson, D., R. Simpson, J. Twicken, G. Tyler, and F. Flasar (2000), Correction to "Initial results from radio occultation measurements with Mars Global Surveyor" by D. P. Hinson et al., *J. Geophys. Res.*, *105*, 1717–1717.

Hinson, D. P., G. L. Tyler, J. L. Hollingsworth, and R. J. Wilson (2001), Radio occultation measurements of forced atmospheric waves on Mars, *J. Geophys. Res.*, *106*, 1463–1480, doi:10.1029/2000JE001291.

Kliore, A. (1992), Radio occultation observations of the ionospheres of Mars and Venus, in *Venus and Mars: Atmospheres, Ionospheres and Solar Wind Interactions*, *Geophys. Monogr. Ser.*, vol. 66, edited by J. Luhmann, M. Tatrallyay, and R. Pepin, pp. 265–276, AGU, Washington, D. C., doi:10.1029/GM066p0265.

Kliore, A., D. L. Cain, G. S. Levy, R. Von Eshleman, G. Fjeldbo, and F. D. Drake (1965), Occultation experiment: Results of the first direct measurement of Mars' atmosphere and ionosphere, *Science*, *149*, 1243–1248, doi:10.1126/science.149.3689.1243.

Krasnopolsky, V. (2002), Mars' upper atmosphere and ionosphere at low, medium, and high solar activities: Implications for evolution of water, *J. Geophys. Res.*, *107*(E12), 5128, doi:10.1029/2001JE001809.

Krymskii, A., T. Breus, N. Ness, H. Acuna, J. Connerney, D. Crider, D. Mitchell, and S. Bauer (2002), Structure of the magnetic field fluxes connected with crustal magnetization and topside ionosphere at Mars, *J. Geophys. Res.*, *107*(A9), 1245, doi:10.1029/2001JA000239.

Ledvina, J. A., Y.-J. Ma, and E. Kallio (2008), Modeling and simulating flowing plasmas and related phenomena, *Space Sci. Rev.*, *139*, 143–189, doi:10.1007/s11214-008-9384-6.

Lewis, S. R., M. Collins, P. L. Read, F. Forget, F. Hourdin, R. Fournier, C. Hourdin, O. Talagrand, and J.-P. Huot (1999), A climate database for Mars, *J. Geophys. Res.*, *104*, 24,177–24,194, doi:10.1029/1999JE001024.

Lindal, G., H. Hotz, D. Sweetnam, Z. Shippony, J. Brendal, G. Hartsell, R. Spear, and W. Michael Jr. (1979), Viking radio occultation measurements of the atmosphere and topography of Mars: Data acquired during 1 Martian year of tracking, *J. Geophys. Res.*, *84*, 8443–8456, doi:10.1029/JB084iB14p08443.

Martinis, C., J. Wilson, and M. Mendillo (2003), Modeling day-to-day ionospheric variability on Mars, *J. Geophys. Res.*, *108*(A10), 1383, doi:10.1029/2003JA009973.

Mendillo, M., G. Hawkins, and J. Klobuchar (1975), A large-scale hole in the ionosphere caused by the launch of Skylab, *Science*, *187*, 343–346, doi:10.1126/science.187.4174.343.

Mendillo, M., J. Baumgardner, D. Allen, J. Foster, J. Holt, G. Ellis, A. Klekociuk, and G. Reber (1987), Spacelag-2 plasma depletion experiments for ionospheric and radio astronomical studies, *Science*, *238*, 1260–1264, doi:10.1126/science.238.4831.1260.

Mendillo, M., S. Smith, J. Wroten, and H. Rishbeth (2003), Simultaneous ionospheric variability on Earth and Mars, *J. Geophys. Res.*, *108*(A12), 1432, doi:10.1029/2003JA009961.

Mendillo, M., P. Withers, D. Hinson, H. Rishbeth, and B. Reinisch (2006), Effects of solar flares on the ionosphere of Mars, *Science*, *311*, 1135–1138, doi:10.1126/science.1122099.

Mendillo, M., S. Smith, A. Coster, P. Erickson, J. Baumgardner, and C. Martinis (2008), Man-made space weather, *Space Weather*, *6*, S09001, doi:10.1029/2008SW000406.

Mendillo, M., J. Wroten, R. Roble, and H. Rishbeth (2010), The equatorial and low-latitude ionosphere within the context of global modeling, *J. Atmos. Sol. Terr. Phys.*, *72*, 358–368, doi:10.1016/j.jastp.2009.03.026.

Moore, L., and M. Mendillo (2007), Are plasma depletions in Saturn's ionosphere a signature of time-dependent water input?, *Geophys. Res. Lett.*, *34*, L12202, doi:10.1029/2007GL029381.

Moore, L., A. Nagy, A. Kliore, I. Müller-Wodarg, J. Richardson, and M. Mendillo (2006a), Cassini radio occultations of Saturn's ionosphere: Model comparisons using a constant water flux, *Geophys. Res. Lett.*, *33*, L22202, doi:10.1029/2006GL027375.

Moore, L., M. Mendillo, C. Martinis, and S. Bailey (2006b), Day-to-day variability of the E layer, *J. Geophys. Res.*, *111*, A06307, doi:10.1029/2005JA011448.

Moore, L., M. Galand, I. Müller-Wodarg, R. Yelle, and M. Mendillo (2008), Plasma temperatures in Saturn's ionosphere, *J. Geophys. Res.*, *113*, A10306, doi:10.1029/2008JA013373.

Moore, L., M. Galand, I. Müller-Wodarg, and M. Mendillo (2009), Response of Saturn's ionosphere to solar radiation: Testing parameterizations for thermal electron heating and secondary ionization processes, *Planet. Space Sci.*, *57*, 1699–1705, doi:10.1016/j.pss.2009.05.001.

Morgan, D., et al. (2011), Dual-spacecraft observations of large-scale magnetic flux ropes in the Martian ionosphere, *J. Geophys. Res.*, *116*, A02319, doi:10.1029/2010JA016134.

Müller-Wodarg, I. C. F., M. Mendillo, R. V. Yelle, and A. D. Aylward (2006), A global circulation model of Saturn's thermosphere, *Icarus*, *180*, 147–160, doi:10.1016/j.icarus.2005.09.002.

Nair, H., M. Allen, A. D. Anbar, Y. L. Yung, and R. T. Clancy (1994), A photochemical model of the Martian atmosphere, *Icarus*, *111*, 124–150.

Najib, D., A. F. Nagy, G. Tóth, and Y. Ma (2011), Three-dimensional, multifluid, high spatial resolution MHD model studies of the solar wind interaction with Mars, *J. Geophys. Res.*, *116*, A05204, doi:10.1029/2010JA016272.

Nicholson, W. P., G. Gronoff, J. Lilensten, A. D. Aylward, and C. Simon (2009), A fast computation of the secondary ion production in the ionosphere of Mars, *Mon. Not. R. Astron. Soc.*, *400*, 369–382, doi:10.1111/j.1365-2966.2009.15463.x.

Nier, A., and M. McElroy (1976), Structure of the neutral upper atmosphere of Mars: Results from Viking 1 and Viking 2, *Science*, *194*, 1298–1300, doi:10.1126/science.194.4271.1298.

Pätzold, M., et al. (2004), MaRS: Mars Express Orbiter Radio Science, in *Mars Express: The Scientific Payload*, *Eur. Space Agency Spec. Publ.*, *ESA SP-1240*, 141–163.

Pätzold, M., S. Tellmann, B. Häusler, D. Hinson, R. Schaa, and G. Tyler (2005), A sporadic third layer in the ionosphere of Mars, *Science*, *310*, 837–839, doi:10.1126/science.1117755.

Picone, J. M., A. E. Hedin, D. P. Drob, and A. C. Aikin (2002), NRLMSISE-00 empirical model of the atmosphere: Statistical comparisons and scientific issues, *J. Geophys. Res.*, *107*(A12), 1468, doi:10.1029/2002JA009430.

Rishbeth, H., and O. K. Garriott (1969), *Introduction to Ionospheric Physics*, *Int. Geophys. Ser.*, vol. 14, Academic, New York.

Rishbeth, H., M. Mendillo, J. Wroten, and R. G. Roble (2009), Day-by-day modelling of the ionospheric F2-layer for year 2002, *J. Atmos. Sol. Terr. Phys.*, *71*, 848–856, doi:10.1016/j.jastp.2009.03.022.

Rohrbaugh, R. P., J. S. Nisbet, E. Bleuler, and J. R. Herman (1979), The effect of energetically produced O_2^+ on the ion temperatures of the Martian thermosphere, *J. Geophys. Res.*, *84*, 3327–3338, doi:10.1029/JA084iA07p03327.

Safaeinili, A., W. Kofman, J. Mouginot, Y. Gim, A. Herique, A. B. Ivanov, J. J. Plaut, and G. Picardi (2007), Estimation of the total electron content of the Martian ionosphere using radar sounder surface echoes, *Geophys. Res. Lett.*, *34*, L23204, doi:10.1029/2007GL032154.

Schunk, R. W., and A. F. Nagy (2000), *Ionospheres*, Cambridge Univ. Press, New York, doi:10.1017/CBO9780511551772.

Schunk, R. W., and A. F. Nagy (2009), *Ionospheres*, 2nd ed., Cambridge Univ. Press, New York, doi:10.1017/CBO9780511635342.

Shinagawa, H., and T. E. Cravens (1989), A one-dimensional multispecies magnetohydrodynamic model of the dayside ionosphere of Mars, *J. Geophys. Res.*, *94*, 6506–6516, doi:10.1029/JA094iA06p06506.

Shinagawa, H., and T. E. Cravens (1992), The ionospheric effects of a weak intrinsic magnetic field at Mars, *J. Geophys. Res.*, *97*, 1027–1035, doi:10.1029/91JE02720.

Singh, R. N., and R. Prasad (1983), Production of dayside ionosphere of Mars, *J. Astrophys. Astron.*, *4*, 261–269, doi:10.1007/BF02714920.

Smith, F. L., III, and C. Smith (1972), Numerical evaluation of Chapman's grazing incidence integral ch (X, χ), *J. Geophys. Res.*, *77*, 3592–3597, doi:10.1029/JA077i019p03592.

Tobiska, W. K. (2004), SOLAR2000 irradiances for climate change, aeronomy, and space systems engineering, *Adv. Space Res.*, *34*, 1736–1746, doi:10.1016/j.asr.2003.06.032.

Verner, D. A., and D. G. Yakovlev (1995), Analytic FITS for partial photoionization cross sections, *Astron. Astrophys. Suppl.*, *109*, 125–133.

Verner, D. A., G. J. Ferland, K. T. Korista, and D. G. Yakovlev (1996), Atomic data for astrophysics. II. New analytic fits for photoionization cross sections of atoms and ions, *Astrophys. J.*, *465*, 487.

Withers, P. (2008), Theoretical models of ionospheric electrodynamics and plasma transport, *J. Geophys. Res.*, *113*, A07301, doi:10.1029/2007JA012918.

Withers, P. (2009), A review of observed variability in the dayside ionosphere of Mars, *Adv. Space Res.*, *44*, 277–307, doi:10.1016/j.asr.2009.04.027.

Withers, P., M. Mendillo, H. Rishbeth, D. Hinson, and J. Arkani-Hamed (2005), Ionospheric characteristics above Martian crustal magnetic anomalies, *Geophys. Res. Lett.*, *32*, L16204, doi:10.1029/2005GL023483.

Withers, P., M. Mendillo, D. Hinson, and K. Cahoy (2008), Physical characteristics and occurrence rates of meteoric plasma layers detected in the Martian ionosphere by the Mars Global Surveyor Radio Science Experiment, *J. Geophys. Res.*, *113*, A12314, doi:10.1029/2008JA013636.

A. Lollo, M. Matta, M. Mendillo, and P. Withers, Department of Astronomy, Boston University, Boston, MA 02215, USA. (alollo@bu.edu; majdm@bu.edu; mendillo@bu.edu; withers@bu.edu)

M. Pätzold and S. Tellmann, Rheinisches Institut für Umweltforschung, Abteilung Planetenforschung, University of Cologne, Cologne D-50931, Germany. (martin.paetzold@uni-koeln.de; stellman@uni-koeln.de)